CHALMERS
UNIVERSITY OF TECHNOLOGY

Direct searches for general dark matter-electron interactions with graphene detectors: Part II. Sensitivity studies

Downloaded from: https://research.chalmers.se, 2024-10-12 07:10 UTC

Citation for the original published paper (version of record):
Catena, R., Emken, T., Matas, M. et al (2023). Direct searches for general dark matter-electron interactions with graphene detectors: Part II.
Sensitivity studies. Physical Review Research, 5(4).
http://dx.doi.org/10.1103/PhysRevResearch.5.043258

N.B. When citing this work, cite the original published paper.

research.chalmers.se offers the possibility of retrieving research publications produced at Chalmers University of Technology. It covers all kind of research output: articles, dissertations, conference papers, reports etc. since 2004. research.chalmers.se is administrated and maintained by Chalmers Library

(article starts on next page)

Direct searches for general dark matter-electron interactions with graphene detectors: Part II. Sensitivity studies

Riccardo Catena,[1,*] Timon Emken,[2,†] Marek Matas,[3,‡] Nicola A. Spaldin,[3,§] and Einar Urdshals[1,‖]
[1]*Chalmers University of Technology, Department of Physics, SE-412 96 Göteborg, Sweden*
[2]*The Oskar Klein Centre, Department of Physics, Stockholm University, AlbaNova, SE-10691 Stockholm, Sweden*
[3]*Department of Materials, ETH Zürich, CH-8093 Zürich, Switzerland*

(Received 6 April 2023; accepted 19 September 2023; published 15 December 2023)

We use a formalism that describes electron ejections from graphenelike targets by dark matter (DM) scattering for general forms of scalar and spin-1/2 DM-electron interactions in combination with state-of-the-art density functional calculations to produce predictions and reach estimates for various possible carbon-based detector designs. Our results indicate the importance of a proper description of the target electronic structure. In addition, we find a strong dependence of the predicted observed signal for different DM candidate masses and interaction types on the detailed geometry and design of the detector. Combined with directional background vetoing, these dependencies will enable the identification of DM particle properties once a signal has been established.

DOI: 10.1103/PhysRevResearch.5.043258

I. INTRODUCTION

In the quest for dark matter (DM), the lack of detection of weakly interacting massive particles (WIMPs) has motivated the exploration of alternative *theoretical* and *experimental* frameworks. On the theoretical side, the focus is gradually shifting towards DM candidates that are lighter than a nucleon [1], and thereby too light to be observed in conventional nuclear recoil experiments [2,3]. On the experimental side, the emphasis is being placed on the search for sub-GeV DM via electronic transitions induced by the scattering of Milky Way DM particles by the electrons bound to a target material [4,5].

The most common target materials used in low-background experiments are liquid argon [6] or xenon [7–9], and semiconductor crystals [4,5,10–17]. In addition, more exotic materials such as Dirac materials [18,19], graphene [20,21], or carbon nanotubes (CNTs) [22–25] have been carefully investigated in this context. All of these targets have an energy threshold of the order of a few eV in common and are therefore sensitive to sub-GeV DM masses. Furthermore, this class of materials can be inherently sensitive to the direction of the incoming DM particle—a feature that would facilitate discrimination of a signal associated with the DM wind direction from any isotropic experimental background. In particular, intrinsically anisotropic materials such as graphene and CNTs are characterized by an enhanced daily modulation of the rate of DM-induced electron ejections—a pattern that is not expected in typical experimental backgrounds. This enhanced modulation results from a strong daily change in the overlap between the kinematically allowed values of the momentum transfer vector, $\mathbf{q}$, and the values of $\mathbf{q}$ that maximize the material "response function" [defined below in Eq. (2)]. Experiments currently in the design or research and development stage that will search for DM-induced electron ejections from graphene sheets or arrays of CNTs include the Princeton Tritium Observatory for Light, Early-Universe, Massive-Neutrino Yield, or PTOLEMY [26–28], as well as the "Graphene-FET" and "Andromeda" projects [29,30]. The Graphene-FET project focuses on utilizing graphene sheets, while Andromeda operates arrays of CNTs.

In a companion work (hereafter referred to as Paper I) [31], we performed state-of-the-art electronic structure calculations for graphene, and we introduced a solid theoretical and computational framework for the accurate modeling of DM-induced electron ejections from graphene-based targets. Our framework combines effective theory methods—used to describe the interaction between DM and electrons in a general manner [32]—with density functional theory (DFT) in order to express the rate of DM-induced electron ejections from graphene-based targets in terms of a single graphene response function. Remarkably, the latter is directly related to the "diagonal part" of the electron momentum density, which by construction is a solid output of DFT [33,34]. We then applied this framework to calculate the expected daily modulation of the rate of DM-induced electron ejections from a hypothetical detector using graphene as a target material.

This work complements Paper I by extending the framework introduced there to the experimentally relevant case of CNTs, and by performing statistically reliable estimates of

*catena@chalmers.se
†timon.emken@fysik.su.se
‡marek.matas@mat.ethz.ch
§nicola.spaldin@mat.ethz.ch
‖urdshals@chalmers.se

Published by the American Physical Society under the terms of the Creative Commons Attribution 4.0 International license. Further distribution of this work must maintain attribution to the author(s) and the published article's title, journal citation, and DOI.

the expected exclusion limits (assuming a null result) and discovery potential (in the case of a positive signal) for both graphene- and CNT-based detectors. Our sensitivity studies provide valuable information for the design stage of next-generation experiments such as PTOLEMY, Graphene-FET, and dark-PMT.

This article is organized as follows. In Sec. II we review our general formalism for modeling the ejection of electrons by the scattering of DM particles in graphene (Paper I), and we extend it to the case of CNTs. In Sec. III, we introduce specific configurations that a graphene or CNT experiment such as PTOLEMY could operate. In Sec. IV, we discuss the statistical framework for the evaluation of the sensitivity and exclusion reach of the detector, and then we apply our formalism to investigate the potential of the discussed configurations in Sec. V. Finally, we conclude in Sec. VI. We complement this work with Appendixes in which we expand on the analytic form of the employed formalism, and we compare possible setups of CNT-based experiments.

II. GENERAL FORMALISM FOR DARK MATTER-INDUCED ELECTRON EJECTIONS IN GRAPHENE DETECTORS

In the complementary work of Paper I, we introduced a general formalism describing DM-induced electron ejections from periodic systems. Unlike in the case of electronic excitations, discussed in our work on semiconductors [35], in Paper I we modeled the final-state electron as a plane wave, which leads to a reduction of the five material response functions found in [35] into a single one. We achieved this result by using an effective theory framework to list all possible interactions that a nonrelativistic scalar or spin-1/2 DM particle can have with the standard model (SM) [32]. This approach also allowed us to write down explicit expressions for the electron ejection rate for selected benchmark models, which are described in Sec. II C of Paper I. Then we applied the general formalism to the case of two-dimensional targets, with a focus on graphene.

To obtain the graphene material response function, two approaches for electronic structure calculation were tested: DFT and tight binding. As has been shown, the tight-binding approach, while working well for capturing crystal effects within a solid, is not internally self-consistent once one aims to obtain a full description of the material on the wave-function level. In that case, an atomic carbon wave function has to be embedded within the formalism, which requires either an inconsistency in the overlap integral values necessary for the correct reconstruction of graphene energy levels, or an unphysical atomic wave function.

While DFT in general provides only an approximation to the individual electronic states, in Paper I we found that the material response function for electronic ejections is proportional to the "diagonal part" of the target electron momentum density, an observable well-motivated and described within this framework. This is why, for the scope of this work, we will use DFT as our framework of choice for obtaining predictions and studying various carbon-based detector designs in more detail.

A. Master formula

In Paper I, we showed that the matrix element describing bound electrons ejected by nonrelativistic DM factorizes into free-particle and material response functions. The free-particle response function $R_{\rm free}$ depends on the properties of the free particles such as the momentum and mass of the ejected electron and the DM particle. We give $R_{\rm free}$ explicitly in Appendix B. The rate of ejected electrons is given by

$$R = \frac{n_\chi N_{\rm cell}}{32\pi^2 m_\chi^2 m_e^2}\int d^3\mathbf{k}'\int dE_e\int d^3\mathbf{q}\int d^3\mathbf{v}\, f_\chi(\mathbf{v})\delta \times\left(\Delta E_e + \frac{q^2}{2m_\chi} - \mathbf{v}\cdot\mathbf{q}\right)R_{\rm free}(\mathbf{k}',\mathbf{q},\mathbf{v})\, W(\mathbf{k}'-\mathbf{q},E_e), \tag{1}$$

where $n_\chi = 0.4\ \mathrm{GeV/cm^3}/m_\chi$ is the DM particle number density, $N_{\rm cell}$ is the number of unit cells in the detector, and m_e and m_χ are the masses of the electron and DM particle, respectively. $\mathbf{k}'$ is the momentum of the final-state free electron, $\mathbf{q}$ is the momentum transferred from the DM particle to the electron, and $\mathbf{v}$ is the initial state velocity of the DM particle. We have defined the electron's energy change as $\Delta E_e \equiv \frac{k'^2}{2m_e} + \Phi - E_e$, with $E_e - \Phi$ being the energy of the initial-state electron relative to a free electron at rest. $\Phi = 4.3$ eV is the work function of graphene, and $E_e \leqslant 0$ eV. The above-mentioned material-specific response function is given as

$$W(\boldsymbol{\ell}, E_e) = \frac{V_{\rm cell}}{(2\pi)^3}\sum_i\int_{\rm BZ}\frac{d^3\mathbf{k}}{(2\pi)^3}\delta(E_e - E_i(\mathbf{k}))|\widetilde{\psi}_{i\mathbf{k}}(\boldsymbol{\ell})|^2, \tag{2}$$

with $V_{\rm cell}$ being the volume of the unit cell, i being the band index, $\mathbf{k}$ being the Brillouin zone momentum (also referred to as crystal momentum), $E_i(\mathbf{k})$ being the energy of an electron in band i with Brillouin zone momentum $\mathbf{k}$, and $\widetilde{\psi}_{i\mathbf{k}}(\boldsymbol{\ell})$ being the momentum space electron wave function with linear momentum $\boldsymbol{\ell}$. In Eq. (1), the velocity distribution of the DM particles gravitationally bound to the galaxy is assumed to be

$$f_\chi(\mathbf{v}) = \frac{1}{N_{\rm esc}\pi^{3/2}v_0^3}\exp\left[-\frac{(\mathbf{v}+\mathbf{v}_e)^2}{v_0^2}\right]\Theta(v_{\rm esc} - |\mathbf{v}+\mathbf{v}_e|), \tag{3}$$

where we use $v_0 = |\mathbf{v}_0| = 238\ \mathrm{km\,s^{-1}}$ [36] for the local standard of rest speed, and $v_{\rm esc} = 544\ \mathrm{km\,s^{-1}}$ [36] for the galactic escape speed. Following [19], the Earth's velocity with respect to the galactic center, $\mathbf{v}_e$, is expressed in a coordinate system with z-axis in the $\mathbf{v}_0 + \mathbf{v}_\odot$ direction. $\mathbf{v}_\odot$ is the Sun's peculiar velocity, and $v_e = |\mathbf{v}_0 + \mathbf{v}_\odot| \simeq 250.5\ \mathrm{km\,s^{-1}}$ [36] is given as

$$\mathbf{v}_e = v_e\begin{pmatrix}\sin\alpha_e\sin\beta\\ \sin\alpha_e\cos\alpha_e(\cos\beta - 1)\\ \cos^2\alpha_e + \sin^2\alpha_e\cos\beta\end{pmatrix},$$

where $\alpha_e = 42^\circ$, $\beta = 2\pi\, t/\mathrm{day}$, and t is the time variable. Finally, the normalization constant is given by

$$N_{\rm esc} \equiv \mathrm{erf}(v_{\rm esc}/v_0) - \frac{2}{\sqrt{\pi}}\frac{v_{\rm esc}}{v_0}\exp\left(-\frac{v_{\rm esc}^2}{v_0^2}\right). \tag{4}$$

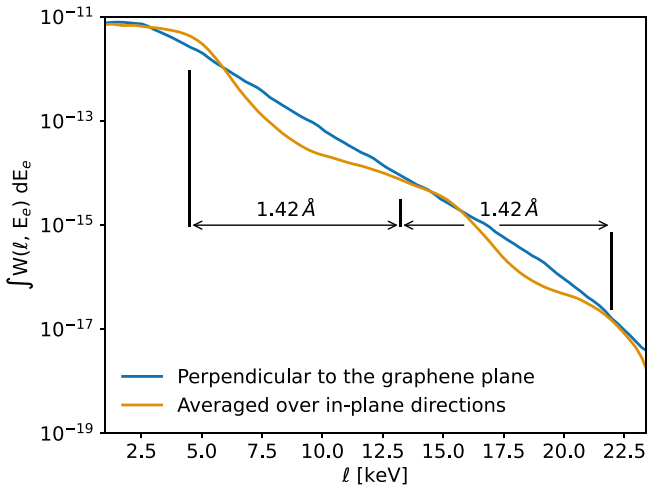

FIG. 1. Graphene response function integrated over energy as a function of the initial electron momentum, ℓ. The blue line represents response function fall-off with momenta that are perpendicular to the graphene sheet, whereas the orange line represents averaged in-sheet momenta. We can see that the in-plane crystal momentum of the lattice with atomic spacing ∼1.42 Å inflates the low-momentum electrons within the sheet.

B. DFT implementation

As discussed above, we use DFT to obtain $W(\boldsymbol{\ell}, E_e)$, expanding the target electron Bloch wave functions $\psi_{i\mathbf{k}}(\mathbf{x})$ in plane waves,

$$\psi_{i\mathbf{k}}(\mathbf{x}) = \frac{1}{\sqrt{V}} \sum_{\mathbf{G}} u_i(\mathbf{k}+\mathbf{G}) e^{i(\mathbf{k}+\mathbf{G})\cdot\mathbf{x}}. \tag{5}$$

These Bloch wave functions are normalized over a finite volume V, while the u_i coefficients obey $\sum_{\mathbf{G}} |u_i(\mathbf{k}+\mathbf{G})| = 1$ for all bands i and all Brillouin zone momenta $\mathbf{k}$. Fourier transforming and squaring Eq. (5) and inserting it in Eq. (2) gives

$$W(\boldsymbol{\ell}, E_e) = V_{\text{cell}} \sum_i \int_{\text{BZ}} \frac{d^3\mathbf{k}}{(2\pi)^3} \delta(E_e - E_i(\mathbf{k})) \times \sum_{\mathbf{G}} |u_i(\mathbf{k}+\mathbf{G})|^2 \delta^{(3)}(\mathbf{k}+\mathbf{G}-\boldsymbol{\ell}). \tag{6}$$

The Bloch coefficients are obtained in a self-consistent field DFT calculation with QUANTUMESPRESSO v.6.4.1 [37–39], and the sum over band indices and the integral over the Brillouin zone momentum are carried out in QEDARK-EFT [40].

DFT directly and self-consistently computes the ground-state electron density, which, as we argued in Paper I, is closely related to $W(\boldsymbol{\ell}, E_e)$, the latter being proportional to the ground-state electron momentum density when band-mixing effects can be neglected. DFT is therefore exceptionally well suited to obtain $W(\boldsymbol{\ell}, E_e)$ for the case of electron ejections from materials. The electron momentum distributions in the directions perpendicular and parallel to the graphene sheet are shown in Fig. 1, where we plot the integrated graphene response as a function of the in-plane and out-of-plane initial electron momentum, ℓ. Note that above approximately 5 keV there are more electrons with a momentum perpendicular to the graphene sheet than parallel to it. As we will see, this observation has an important impact on our predictions.

C. Extension to carbon nanotubes

In this section, we extend the above formalism to the important case of electron ejections by DM scattering in carbon nanotubes. This study is relevant for the development of Andromeda, which will search for DM with arrays of single- or multiwall metallic carbon nanotubes. Furthermore, this detector design has been shown to outperform noncurved graphene sheets for the complementary cosmic neutrino background search due to the Heisenberg uncertainty final-state spectrum smearing [28].

Carbon nanotubes are cylindrical tubes with walls of single or a few atom thickness and a radius of $R_{\text{tube}} \approx 10$ nm. The electronic structure of carbon nanotubes can be modeled using DFT, taking effects of interactions between tubes into account. However, we leave this DFT calculation for future work, and use an approximate expression for the response function of carbon nanotubes that we obtain from that of graphene as explained below.

We start by noticing that a single-wall carbon nanotube can be approximated by the superposition of n_s tangential graphene sheets. This geometrical approximation is kinematically well-motivated as the typical momentum of the initial-state electrons is around a few keV and above, which corresponds to a de Broglie wavelength of $\lambda \lesssim 1$ nm. Since $\lambda \ll R_{\text{tube}}$, the target electrons do not resolve the curvature of the tubes, and segments of the tube walls can be approximated as locally flat and thus described by tangential planes. As a result, the rate of electron ejections by DM scattering in carbon nanotubes can be approximated by the sum of contributions from n_s tangential planes, each of mass $1/n_s$ times the mass of the nanotube.

The n_s tangential planes used in this approximation can be obtained through subsequent, active rotations of a reference graphene sheet. Let us denote by $\Omega_{(j)}$, $j = 1, \ldots, n_s$ the matrix that represents the rotation associated with the jth tangential plane. Under $\Omega_{(j)}$ the Bloch wave function $\psi_{i\mathbf{x}}(\mathbf{x})$ in Eq. (5) transforms as follows:

$$\psi_{i\mathbf{k}}(\mathbf{x}) \longrightarrow \psi'_{i\mathbf{k}}(\mathbf{x}) = \psi_{i\mathbf{k}}\big(\Omega_{(j)}^{-1}\mathbf{x}\big), \tag{7}$$

which implies

$$|\widetilde{\psi}_{i\mathbf{k}}(\boldsymbol{\ell})|^2 \longrightarrow |\widetilde{\psi}'_{i\mathbf{k}}(\boldsymbol{\ell})|^2 = (2\pi)^3 \sum_{\mathbf{G}} |u_i(\mathbf{k}+\mathbf{G})|^2 \delta^{(3)}(\Omega_{(j)}(\mathbf{k}+\mathbf{G}) - \boldsymbol{\ell}). \tag{8}$$

By using

$$\delta^{(3)}(\Omega_{(j)}(\mathbf{k}+\mathbf{G}) - \boldsymbol{\ell}) = \delta^{(3)}\big(\mathbf{k}+\mathbf{G} - \Omega_{(j)}^{-1}\boldsymbol{\ell}\big), \tag{9}$$

we can write the response function of a rotated graphene sheet as

$$W(\boldsymbol{\ell}, E_e) \longrightarrow W'_{(j)}(\boldsymbol{\ell}, E_e) = W\big(\Omega_{(j)}^{-1}\boldsymbol{\ell}, E_e\big), \tag{10}$$

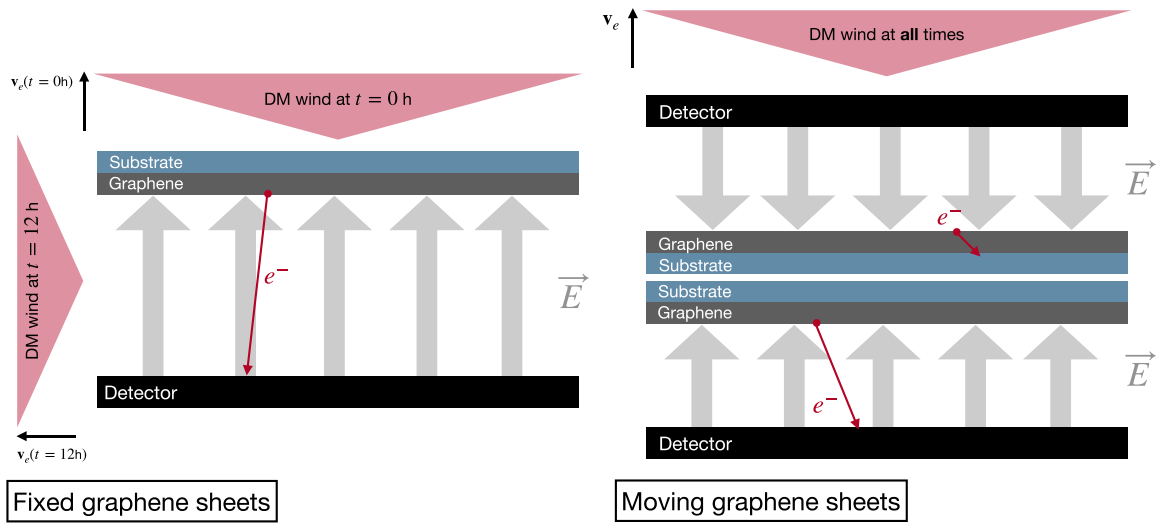

FIG. 2. Schematics of experimental setups with graphene sheet targets. The graphene sheet (dark gray) is grown on a substrate (blue). The electric field in the vacuum surrounding the sheet is shown with gray arrows. Electrons ejected from the sheet are accelerated by the electric field as indicated by the red arrow. Left: Setup in which graphene sheets are fixed in the laboratory. Right: Setup in which graphene sheets are tracking $\mathbf{v}_e$.

and we approximate the response function of a single nanotube as

$$W_{\text{tube}}(\boldsymbol{\ell}, E_e) \approx \sum_{j=1}^{n_s} \frac{W\left(\Omega_{(j)}^{-1}\boldsymbol{\ell}, E_e\right)}{n_s}, \tag{11}$$

where the sum runs over the number of tangential planes used in the approximation. In our calculations, we take the limit of an infinite number of planes, $n_s \to \infty$, which implies

$$W_{\text{tube}}(\boldsymbol{\ell}, E_e) \approx \frac{1}{2\pi} \int d\phi\, W(|\boldsymbol{\ell}|\hat{\boldsymbol{n}}, E_e), \tag{12}$$

where $\hat{\boldsymbol{n}} = (\cos\phi \sin\theta, \sin\phi \sin\theta, \cos\theta)$, $\cos\theta = \boldsymbol{\ell} \cdot \hat{\mathbf{z}}/|\boldsymbol{\ell}|$, $\hat{\mathbf{z}}$ is a unit vector in the direction of the symmetry axis of the nanotube, and ϕ is the associated azimuthal angle. In practice, we perform the integral in Eq. (12) together with the velocity and momentum transfer integrals in Eq. (1) by random sampling ϕ with Monte Carlo methods.

III. EXPERIMENTAL SETTINGS FOR GRAPHENE-BASED DARK MATTER DETECTORS

In the laboratory frame, the flux of DM particles through the Earth, that is, the so-called DM wind, peaks at $\mathbf{v} = -\mathbf{v}_e$, as one can see from Eq. (3). Since $\mathbf{v}_e$ varies during the day, the rate of electron ejections by DM scattering is expected to modulate correspondingly over a period of 24 h. For a given $\mathbf{k}'$, the amplitude of this daily modulation is large when the kinematically allowed regions for $\mathbf{q}$, found by solving the δ-function constraint in Eq. (1), and the regions where $\mathbf{k}' - \mathbf{q}$ maximizes $W(\mathbf{k}' - \mathbf{q})$, have a nontrivial overlap at a given time, and a marginal overlap 12 h later. Whether the overlap between peaks of W and kinematically allowed regions in $\mathbf{q}$-space follows this time evolution depends on the initial angle between $\mathbf{v}_e$ and the symmetry axis of the assumed target material. Consequently, anisotropic materials characterized by an angle-dependent response function can be used to amplify the expected daily modulation of the electron ejection rate by an appropriate choice of detector orientation. Importantly, none of the known experimental backgrounds is expected to exhibit a similar daily modulation, which would therefore be a smoking gun for DM discovery. In this article, we consider two experimental setups that are in principle capable of detecting this daily modulation. The two setups can be realized by using multilayer graphene or carbon nanotube array detectors. Both targets have an anisotropic response function (see Secs. II B and II C).

In the first setup, we consider an anisotropic detector fixed in the laboratory frame, so that the angle between the detector's symmetry axis, e.g., the z-axis $\hat{\mathbf{z}}$, and the direction of $\mathbf{v}_e$ varies during the day, producing a daily modulation in the DM-induced signal. Both graphene and carbon nanotubes can be used to realize this setup, as shown in the left panels of Figs. 2 and 3 for graphene and carbon nanotubes, respectively.

In a second setup, we consider a pair of identical anisotropic detectors mounted with opposite orientations onto a platform that tracks the DM wind. For this setup, a smoking gun signal for DM discovery would be a statistically significant difference in the number of events in the two detectors. The right panel of Fig. 2 shows a realization of this setup based on graphene sheets, while the right panel in Fig. 3 illustrates a realization of the same setup based on carbon nanotubes. The latter will be employed by Andromeda [30].

As far as the detection of the ejected electrons is concerned, we assume that this can be achieved by drifting the ejected electrons in an external electric field. When electrons are ejected from graphene sheets (solid gray stripe in Fig. 2), we assume that all electrons ejected into the electric field will drift to the detector, whereas the electrons ejected into the substrate (light blue band in Fig. 2) will be absorbed by the substrate and not detected. When electrons are ejected from CNTs (vertical honeycombed structures attached to the light blue substrate in Fig. 3), they need to propagate through the CNT array in order to be detected. In spherical coordinates, with

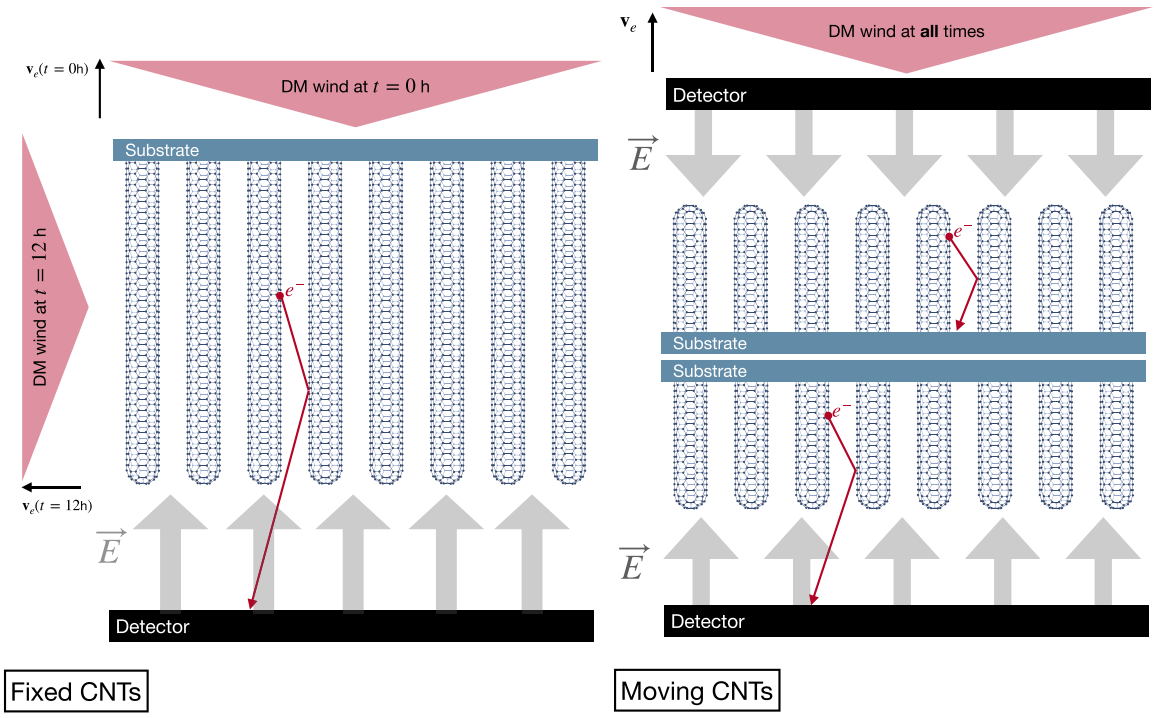

FIG. 3. Schematics of experimental setups with carbon nanotubes (CNTs) as targets. The CNTs are grown on a substrate (blue). The electric field in the vacuum surrounding the sheet is shown with gray arrows. Electrons ejected into the field are indicated by the red arrow. Left: Setup in which the CNTs are fixed in the laboratory. Right: Setup in which the CNTs are tracking $\mathbf{v}_e$.

the CNTs (graphene sheets) aligned with (perpendicular to) the z-axis and electrons leaving the CNTs (graphene sheets) in the negative z-direction are detected whereas the electrons leaving the CNTs (graphene sheets) in the positive z-direction are not, the rate of detected electrons, $\mathscr{R}$, can finally be written as follows:

$$\mathscr{R} = \int d\,k' d\,\theta' d\,\phi' \sin\theta' \frac{d^3 R}{dk' d\cos\theta'\, d\phi'} f(k', \theta', \phi'), \quad (13)$$

where

$$\frac{d^3 R}{dk' d\cos\theta'\, d\phi'}(\mathbf{k}') = \frac{n_\chi (k')^2 N_{\text{cell}}}{32\pi^2 m_\chi^2 m_e^2} \int dE_e \int d^3\mathbf{q} \int d^3\mathbf{v}\, f_\chi(\mathbf{v})\delta \times \left(\Delta E_e + \frac{q^2}{2m_\chi} - \mathbf{v}\cdot\mathbf{q}\right) R_{\text{free}}(\mathbf{k}', \mathbf{q}, \mathbf{v}) \times W(\mathbf{k}' - \mathbf{q}, E_e) \quad (14)$$

is the triple differential electron ejection rate, and $\{k', \theta', \phi'\}$ are the spherical coordinates of the final-state electron momentum. $f(k', \theta', \phi')$ is the probability of an electron ejected with momentum k' and propagating in direction $\{\theta', \phi'\}$ being detected. The exact form of $f(k', \theta', \phi')$ depends heavily on the geometry of the considered detector (typical CNT length, diameter, density, etc.). Since the exact geometry is not yet set, we chose to use a simplistic distribution

$$f(k', \theta', \phi') = \Theta(\theta' - \theta^*), \quad (15)$$

where θ^* is the cutoff angle below which an electron is not detected. In this work, we use $\theta^* = 100^\circ$ for CNTs to obtain an asymmetry in the number of events reported by the two detectors and a differential rate comparable to that found in Ref. [24]. For graphene-based experiments, we use $\theta^* = 90^\circ$.

IV. SENSITIVITY STUDIES: STATISTICAL FRAMEWORK

In this section, we introduce the statistical framework we use to assess the expected performance of the two experimental setups described in the previous section. For each setup, we are interested in two possible experimental outcomes. In the first, the experiment reports the detection of DM particles with a statistical significance corresponding to three standard deviations, i.e., "3σ." In the second, we assume that the number of observed events is too small to report a DM particle discovery, and should therefore be interpreted as a "null result." We explore the implications of the two experimental outcomes by using different test statistics, as we briefly explain below.

Let us start by focusing on the scenario in which DM particles have actually been detected. The experimental setups discussed above would establish such a discovery through the observation of an asymmetry in the number of events reported in different detector components, or in different periods of the day. For the fixed target setup, the detection of DM particles would imply an asymmetry in the number of events recorded in the 12 h of the day around the expected times of maximum and minimum rate.[1] For the moving twin experiment setup, the discovery of DM would imply an asymmetry in the

[1]In practice this requires recording events in 24 one-hour-wide bins, sorting them, and taking the 12 bins with the highest number of events to contribute to n_+ and the 12 bins with the lowest number of events to contribute to n_-.

TABLE I. Interaction operators defining the nonrelativistic effective theory of spin 0 and 1/2 DM-electron interactions [32]. $\mathbf{S}_e$ ($\mathbf{S}_\chi$) is the electron (DM) spin, $\mathbf{v}_{\rm el}^\perp = \mathbf{v} - \boldsymbol{\ell}/m_e - \mathbf{q}/(2\mu_{\chi e})$, where $\mu_{\chi e}$ is the DM-electron reduced mass, $\mathbf{v}_{\rm el}^\perp$ is the relative transverse velocity, and $\mathbb{1}_{\chi e}$ is the identity in the DM-electron spin space. In the case of elastic scattering, $\mathbf{v}_{\rm el}^\perp \cdot \mathbf{q} = \mathbf{0}$.

$O_1 = \mathbb{1}_{\chi e}$	$O_9 = i\mathbf{S}_\chi \cdot (\mathbf{S}_e \times \frac{\mathbf{q}}{m_e})$
$O_3 = i\mathbf{S}_e \cdot (\frac{\mathbf{q}}{m_e} \times \mathbf{v}_{\rm el}^\perp)$	$O_{10} = i\mathbf{S}_e \cdot \frac{\mathbf{q}}{m_e}$
$O_4 = \mathbf{S}_\chi \cdot \mathbf{S}_e$	$O_{11} = i\mathbf{S}_\chi \cdot \frac{\mathbf{q}}{m_e}$
$O_5 = i\mathbf{S}_\chi \cdot (\frac{\mathbf{q}}{m_e} \times \mathbf{v}_{\rm el}^\perp)$	$O_{12} = \mathbf{S}_\chi \cdot (\mathbf{S}_e \times \mathbf{v}_{\rm el}^\perp)$
$O_6 = (\mathbf{S}_\chi \cdot \frac{\mathbf{q}}{m_e})(\mathbf{S}_e \cdot \frac{\mathbf{q}}{m_e})$	$O_{13} = i(\mathbf{S}_\chi \cdot \mathbf{v}_{\rm el}^\perp)(\mathbf{S}_e \cdot \frac{\mathbf{q}}{m_e})$
$O_7 = \mathbf{S}_e \cdot \mathbf{v}_{\rm el}^\perp$	$O_{14} = i(\mathbf{S}_\chi \cdot \frac{\mathbf{q}}{m_e})(\mathbf{S}_e \cdot \mathbf{v}_{\rm el}^\perp)$
$O_8 = \mathbf{S}_\chi \cdot \mathbf{v}_{\rm el}^\perp$	$O_{15} = iO_{11}[(\mathbf{S}_e \times \mathbf{v}_{\rm el}^\perp) \cdot \frac{\mathbf{q}}{m_e}]$

number of events observed in the two detector components. Let us now denote by n_+ and n_-, $n_+ \geqslant n_-$, the number of counts recorded in the two "regions of interests," i.e., in the time periods/detector components introduced above, and by $n_+ - n_-$ the associated asymmetry. Furthermore, let $E[n_\pm] = \mu s_\pm + \theta_\pm$ be the expected value of $n_\pm$, where $\theta_\pm$ ($\mu s_\pm$) is the expected number of background (DM signal) events in the given region of interest, while μ is the "strength parameter," i.e., c_i^2 for the operators in Table I and g/Λ or g/Λ^2 in the case of dipole and anapole interactions, respectively. $s_\pm$ is the expected number of DM signal events in the given region of interest for $\mu = 1$. For all interactions, we calculate $\mu s_\pm$ by integrating the rate formula we obtained in the previous sections. With this notation, we can write the probability to record $n_\pm$ counts given the expectation $E[n_\pm]$, i.e., given $(\mu, \theta_\pm)$, as follows:

$$\mathscr{P}_\pm(\mu, \theta_\pm) = \frac{e^{-(\mu s_\pm + \theta_\pm)}}{n_\pm!} (\mu s_\pm + \theta_\pm)^{n_\pm} \to \frac{1}{\sqrt{2\pi\sigma_\pm^2}} \exp\left[-\frac{1}{2}\left(\frac{\mu s_\pm + \theta_\pm - n_\pm}{\sigma_\pm}\right)^2\right], \tag{16}$$

where in the second line $E[n_\pm] \gg 1$ and $\sigma_\pm^2 = E[n_\pm]$. To eliminate $n_\pm$ from the equations, we now introduce a specific value for the strength parameter, μ', implicitly defined via

$$n_+ - n_- \equiv \mu'(s_+ - s_-). \tag{17}$$

In an actual experiment, μ' would be the unknown value of μ that underlies the data, whereas in a Monte Carlo simulation, μ' is the benchmark value of μ from which data are sampled. Since the probability density function of the difference of the two normal random variables n_+ and n_- is a normal random variable with expectation value $E[n_+] - E[n_-]$ and variance $\sigma^2 = \sigma_+^2 + \sigma_-^2$, the probability of observing an asymmetry $n_+ - n_-$ given μ and $\theta \equiv \theta_+ + \theta_-$, $\theta_+ = \theta_-$, is proportional to the likelihood function

$$\mathscr{L}(\mu, \theta) = \exp\left[-\frac{1}{2}(\mu - \mu')^2\left(\frac{s_+ - s_-}{\sigma}\right)^2\right]. \tag{18}$$

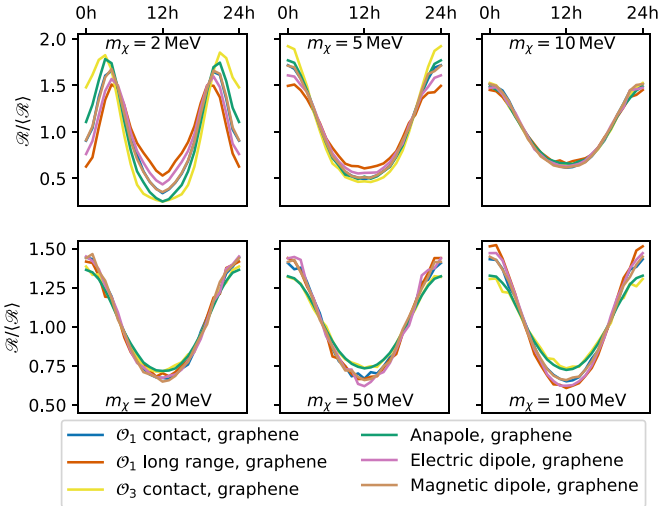

FIG. 4. Daily modulation pattern of detectable electrons in the fixed graphene sheets setup (Fig. 2, left panel) for O_1 contact interaction (blue), O_1 long-range interaction (red), O_3 contact interaction (yellow), the anapole interaction (green), the electric dipole interaction (magenta), and the magnetic dipole interaction (brown). The mass of the DM particle increases from 2 MeV in the top left corner, to 100 MeV in the bottom right corner. When compared to other detector setups, it is easier to recognize a DM signal (since all DM candidates provide a similar signal) but harder to distinguish different interaction models once a signal is detected.

We use Eq. (18) to introduce the test statistics q_0 defined as

$$q_0 = \begin{cases} -2\ln\frac{\mathscr{L}(0,\theta)}{\mathscr{L}(\mu',\theta)} = \frac{(s_+ - s_-)^2\mu'^2}{\theta} & \text{for } \mu' \geqslant 0, \\ 0 & \text{for } \mu' < 0. \end{cases} \tag{19}$$

Here, we neglect statistical fluctuations in the number of background events, and we set θ to its expectation value. For $\mu' = 0$, q_0 obeys a "half chi-square" distribution with one degree of freedom, whereas for $\mu' \neq 0$ it follows a noncentral chi-square distribution [41]. Consequently, we can use q_0 to express the statistical significance for DM particle discovery[2] as $Z = \sqrt{q_0}$ [41]. Notice that $\mathscr{L}(0, \theta) < \mathscr{L}(\mu', \theta)$ when $\mu' \neq 0$ underlies the data. Furthermore, the larger μ' is, the larger is Z, and, therefore, the better one can reject the null hypothesis, i.e., $\mu = 0$ in favor of the alternative hypothesis, $\mu = \mu'$. By obtaining the μ' for which $\sqrt{q_0} = 3$, we find the smallest strength parameter, or coupling constant value, that can be measured with a statistical significance corresponding to "3σ."

As a second experimental outcome, we consider the one in which the observed asymmetry $n_+ - n_-$ is too small to report a DM particle discovery. If an asymmetry in the total number of recorded events, $n_- + n_+$, cannot be established, the experimental data can still be used to exclude values of the coupling constants c_i^2, g/Λ, or g/Λ^2 that would imply $E[n_- + n_+] >$

[2]Significance, Z, and p-value are related by $Z \equiv \Phi^{-1}(1 - p)$, where Φ is the cumulative distribution function of a normal distribution with mean 0 and variance 1 [41] (i.e., the standard normal distribution).

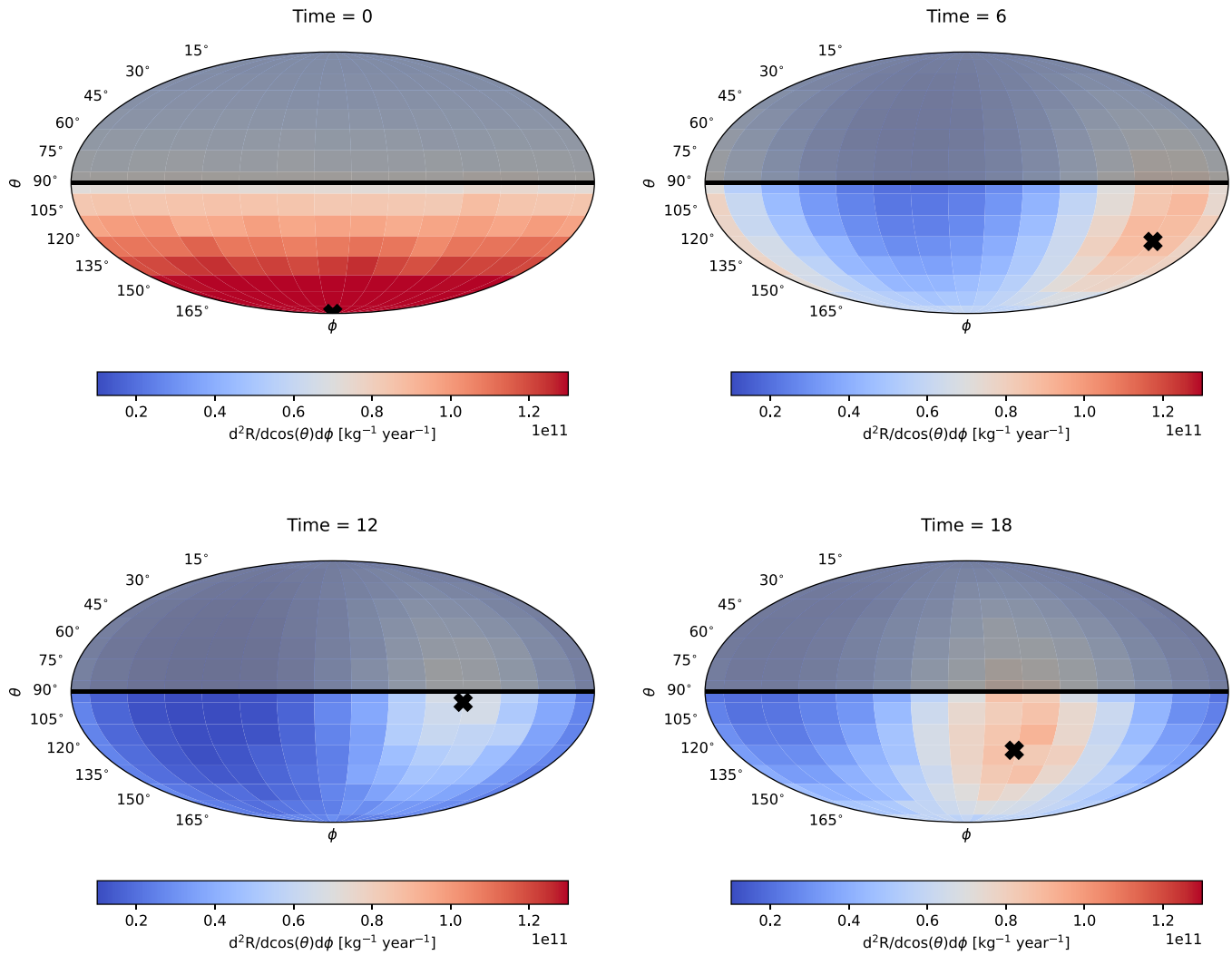

FIG. 5. Projection plot for the magnetic dipole interaction for graphene sheets, $m_\chi = 5$ MeV, for different times (in hours) throughout the day. At time = 0 h, the DM wind (denoted as a black cross) is perpendicular to the graphene sheet, which is shown as a solid black line at $\theta = 90^\circ$. The shaded region denotes the substrate where ejected electrons will not be detected. This plot represents a family of solutions for which the operator does not contain the term $\frac{\mathbf{q}}{m_e} \times \mathbf{v}_{\rm el}^{\perp}|_{\ell=0} = \frac{\mathbf{q}}{m_e} \times \mathbf{v}$, and therefore $\mathbf{q}$ in the direction of $\mathbf{v}$ is not suppressed. The DM wind direction and ejected electron momentum are therefore similar.

$n_- + n_+$. Conservatively, here we assume that all recorded events are due to DM, i.e., $E[n_- + n_+] = \mu(s_- + s_+)$, and we do not perform any background subtraction. We then compute 90% confidence level (C.L.) exclusion limits on μ, or, equivalently, on c_i^2, g/Λ, or g/Λ^2, by imposing that the probability of observing $n_- + n_+$ or fewer events when our expectation is $E[n_- + n_+] = \mu(s_- + s_+)$ is 10%. We therefore solve

$$e^{-\mu(s_- + s_+)} \sum_{i=0}^{n_- + n_+} \frac{\mu(s_- + s_+)^i}{i!} = 0.1 \tag{20}$$

for μ for each of the four experimental setups introduced above. In this analysis, we assume two reference data samples: (i) $n_- + n_+ = 0$, and (ii) $n_- + n_+ = \mu'(s_- + s_+) + \theta$, where μ' and θ solve the equation $\sqrt{q_0} = 3$, as explained above. The first sample implies the strongest exclusion limits one can expect, whereas the second one corresponds to a scenario where DM is at the threshold of discovery.

V. SENSITIVITY STUDIES: EXPECTED EJECTION RATES, EXCLUSION LIMITS, AND DISCOVERY POTENTIAL

In this section, we numerically evaluate the ejection rates from graphene sheets and carbon nanotubes for various models of DM, and we determine the sensitivity of selected detector setups within these models.

A. Ejection rate for graphene sheets

For the case of a static graphene sheet fixed in the laboratory [Fig. 2 (left)], the rate of ejected electrons varies throughout the day as the orientation of the DM wind changes. As we showed already in Paper I, this change depends on the DM mass and on the form of the DM-electron interaction; we reproduce the results of Paper I in Fig. 4. The displayed interactions are O_1 (contact and long-range interaction), O_3 (contact interaction), as well as the anapole, electric dipole, and magnetic dipole interactions. DM mass ranges from 2

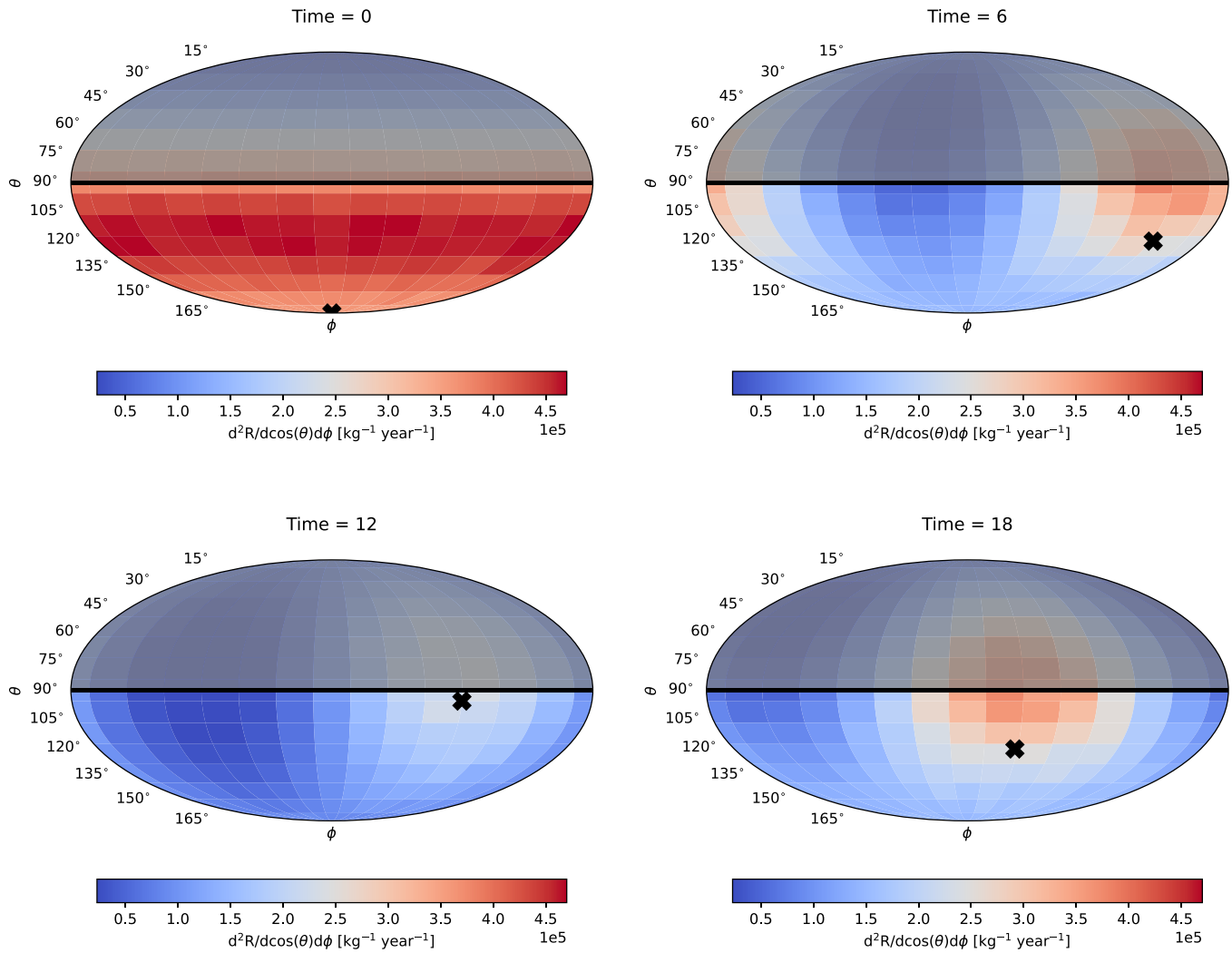

FIG. 6. Projection plot for O_3 contact interaction for graphene sheets, $m_\chi = 5$ MeV, for different times throughout the day. At time = 0 h, DM wind (denoted as a black cross) is perpendicular to the graphene sheet, which is shown as a solid black line at $\theta = 90^\circ$. The shaded region denotes the substrate where ejected electrons will not be detected. This plot represents a family of solutions for which the operator contains the term $\frac{\mathbf{q}}{m_e} \times \mathbf{v}_{\rm el}^{\perp}|_{\ell=0} = \frac{\mathbf{q}}{m_e} \times \mathbf{v}$, suppressing $\mathbf{q}$ in the direction of $\mathbf{v}$ and offsetting the direction of the ejected electron momentum from that of the DM wind.

to 100 MeV. We see that the modulation curves are qualitatively similar for the considered interactions and for most DM masses with a maximum at time = 0 h and a minimum at time = 12 h. However, for the low DM mass of 2 MeV, we see that the peaks are displaced from time = 0 h to around time = 3 h and that the precise location of the peak depends somewhat on the interaction type. As discussed in the associated Paper I, the displacement of the peak at 2 MeV is due to the momentum distribution of the most loosely bound electrons in the graphene sheet.

Figures 5 and 6 show a two-dimensional projection of the rate integrated over all final-state electron energies as a function of time for the magnetic dipole and the O_3 interactions. From these plots, we can see a preferential direction of the ejected electrons as well as the overall rate modulation for various angular orientations along with the direction of the DM wind (denoted as a black marker).

As can be seen from Eq. (14), the final differential rate depends on four independent contributing factors, namely the distribution of the DM velocities, kinematic constraints imposed by energy conservation, the properties of the material entering through the material response function W, and the form of the interaction entering through the free-particle response function $R_{\rm free}$.

The DM velocity distribution in Eq. (3) is the truncated Maxwell-Boltzmann distribution typically assumed within the standard halo model (SHM) [36]. It peaks at $\mathbf{v} = -\mathbf{v}_e$ and is exponentially suppressed for velocities of $\mathbf{v}$ away from $-\mathbf{v}_e$. The associated speed distribution is found by integrating Eq. (3) over angles, and multiplying by $v^2 = |\mathbf{v}|^2$. The minimum speed a DM particle must have in order to transfer a momentum q and deposit an energy ΔE_e is

$$v_{\rm min} = \frac{\Delta E_e}{q} + \frac{q}{2m_\chi}, \tag{21}$$

as one can see by setting to zero the argument of the Dirac δ function in Eq. (1). The same δ function also implies that the integrand in the electron ejection rate peaks at $v = v_{\rm min}$, and

hence for $\mathbf{v}$ parallel to $\mathbf{q}$, as long as $v_{\rm min}$ is larger than the most probable speed for all allowed q and ΔE_e. This is the case for m_χ below a few MeV.

As can be seen from Fig. 1, the properties of the electronic wave function in the material favor states where the modulus of the initial-state electron momentum, $|\boldsymbol{\ell}| = |\mathbf{k}' - \mathbf{q}|$, is around 4 keV. Let us now denote by $\zeta \sim 4$ keV the "typical" value of $|\boldsymbol{\ell}|$ preferred by the electronic properties of graphene. For $m_\chi > \zeta/v_{\rm max}$, we find that ζ is smaller than the "typical" momentum transferred in a DM-electron interaction,[3] $q_{\rm typ} \equiv m_\chi v_{\rm max}$, where $v_{\rm max}$ is the maximum possible speed of a DM particle gravitationally bound to the Milky Way. For $\zeta < q_{\rm typ}$, we also find that the angle between $\mathbf{k}'$ and $\mathbf{q}$ is expected to be smaller than $\pi/2$.[4] This in turn implies that the angle between $\mathbf{v}$ and $\mathbf{k}'$ is smaller than $\pi/2$ when the initial velocity $\mathbf{v}$ is aligned with $\mathbf{q}$, i.e., for DM masses below a few MeV. As a result, we predict a forward-backward asymmetry in the rate of DM-induced electron ejections, and therefore a directional sensitivity to the incoming DM wind for graphene detectors. An illustration of this is provided in Fig. 5.

Of course, this feature holds only if its effect is not countered by the fourth term in Eq. (14), the DM response function $R_{\rm free}$. Almost all the effective operators shown in Table I do not suppress the ejection of electrons along the direction of the DM wind with the exception of the operators O_3 and O_5. These contain the term $\frac{\mathbf{q}}{m_e} \times \mathbf{v}_{\rm el}^{\perp}|_{\boldsymbol{\ell}=0} = \frac{\mathbf{q}}{m_e} \times \mathbf{v}$, which disfavors a parallel orientation of $\mathbf{v}$ and $\mathbf{q}$ and, in combination with the previously discussed terms, favors a rate offset from the direction of the DM wind (as can be seen in Fig. 6).

B. Ejection rate for carbon nanotubes

In this subsection, we discuss the numerical results obtained for the carbon-nanotube experiments, both in a static setup observing daily modulation as well as in a second, moving setup with two identical detector arms in which one tracks the direction of the DM wind and the second is aimed in a different direction to establish a rate difference.

The angular dependence of the ejected electrons is more complicated for CNTs than for graphene sheets, as in this case there are two competing effects, each dominating a different interaction energy regime. On the one hand, due to the additional crystal momentum within the graphene (CNT) sheet, there are more electron states with large out-of-plane lying momentum than in-plane (as discussed in the previous section). So, generally, interactions in which DM is oriented perpendicularly to the sheet are preferred over those in which DM arrives parallel to the sheet. The preference is particularly strong for low DM candidate masses, since they have low energy and thus, due to energy-momentum conservation, they require an electron with a large momentum in order to overcome the work function. Large-mass candidates carry enough kinetic energy on their own and rely less on the initial momentum of the target electron. However, this effect is countered in the case of CNTs by the fact that the acceptance of the detector limits the allowed angles of ejected electrons, which must be oriented close to along the direction of the tube walls to escape. This, together with the fact that long-range interactions carry an additional factor of $\sim\frac{1}{q^2}$ suppressing large momentum transfers, causes a nontrivial pattern to emerge in the daily modulation plots for various masses and interaction types.

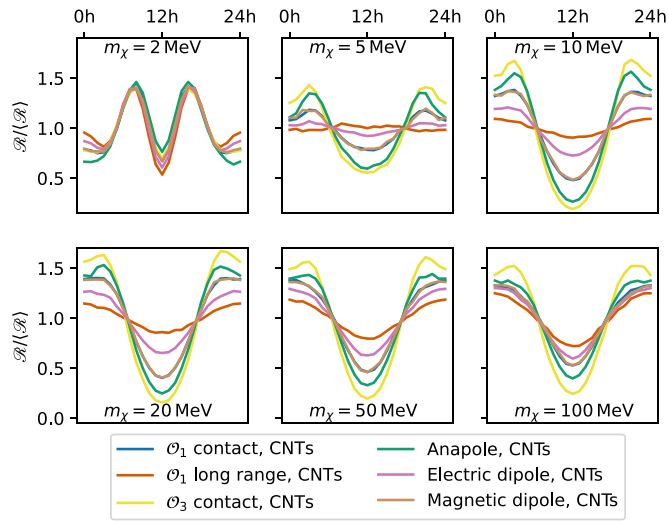

FIG. 7. Same as Fig. 4, but for the case of fixed carbon nanotubes. We see that for $m_\chi = 2$ MeV the rate is maximal around time = 6 h and time = 18 h for all interactions. For larger masses, however, the daily modulation pattern strongly differs between different interaction types. Interestingly, the O_1 long-range and electric dipole interactions produce a daily modulation pattern that is largely flat at $m_\chi = 5$ MeV, making establishing a daily modulation difficult.

In Fig. 7, we show the daily modulation plot for the O_1 operator (both contact and long-range interactions), O_3 operator (contact interaction), and the anapole, electric, and magnetic dipole interactions. For $m_\chi = 2$ MeV, the modulation curves are qualitatively similar for all considered interactions, with maxima around time = 6 h and time = 18 h, when the DM wind forms a roughly 35° degree angle with the tube axis. For $m_\chi = 100$ MeV, the modulation curves are also mostly qualitatively similar with minima around time = 12 h for all plotted interactions and maxima at time = 0 h for all the interactions with the exception of O_3 contact, whose produced rate-maxima are displaced. For masses between 2 and 100 MeV, we see qualitative differences between the interactions. Note in particular that for the O_1 long-range and the electric dipole interactions, the curves flatten out around

[3]By imposing $v_{\rm min} < v_{\rm max}$, one finds that $q_{\rm min} < q < q_{\rm max}$, where

$$q_{\rm min} = m_\chi v_{\rm max} - \sqrt{m_\chi^2 v_{\rm max}^2 - 2m_\chi(\Phi - E_e)},$$
$$q_{\rm max} = m_\chi v_{\rm max} + \sqrt{m_\chi^2 v_{\rm max}^2 - 2m_\chi(\Phi - E_e)}.$$

[4]The vectors $\boldsymbol{\ell}$, $\mathbf{q}$, and $\mathbf{k}'$ must form a triangle. It is instructive to draw this triangle placing the vertex at the intersection of $\boldsymbol{\ell}$ and $\mathbf{q}$ at the center of a circle of radius $|\boldsymbol{\ell}|$. Doing so, we also set $|\boldsymbol{\ell}|$ and $|\mathbf{q}|$ to their representative values, ζ and $q_{\rm typ}$, respectively. For $\zeta < q_{\rm typ}$, the angle between $\mathbf{k}'$ and $\mathbf{q}$ (with $|\mathbf{q}| = q_{\rm typ}$) is maximum when $\mathbf{k}'$ is tangent to the above circle of radius $|\boldsymbol{\ell}| = \zeta$. This occurs when the angle between the vectors $\mathbf{k}'$ and $\boldsymbol{\ell}$ is equal to $\pi/2$, and therefore the angle between $\mathbf{q}$ and $\mathbf{k}'$ is less than $\pi/2$.

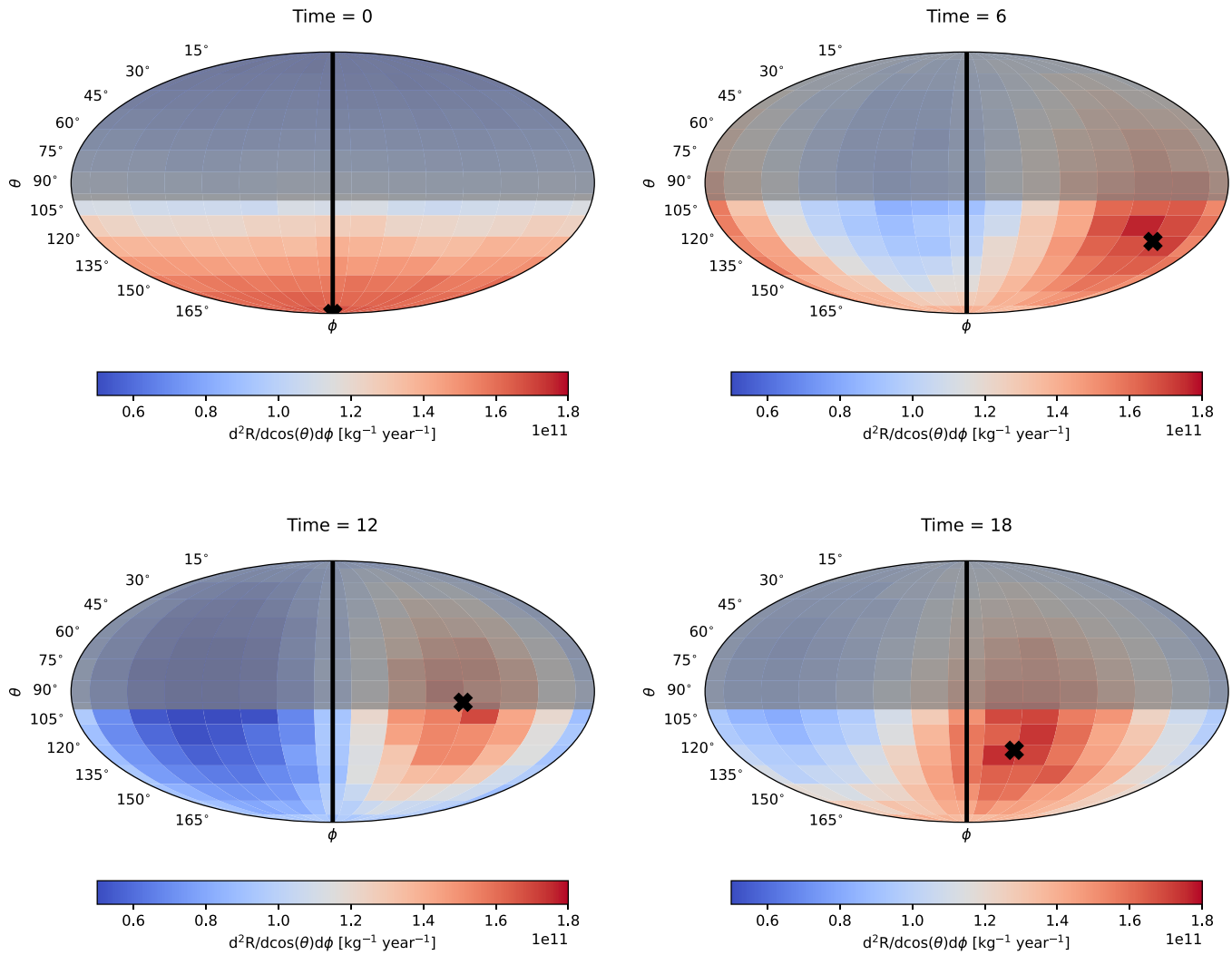

FIG. 8. Same as Fig. 5, but for a detector made of CNTs. The vertical black line corresponds to the orientation of the tube axis.

$m_\chi = 5$ MeV (due to the balancing of the two competing directional effects discussed in the previous paragraph). As will be discussed in Sec. V C, this causes an experiment searching for a daily modulation signal to lose sensitivity at this mass, and is seen as peaks in the yellow curves around $m_\chi = 5$ MeV in the top right and bottom left panels of Fig. 10.

From the comparison of Figs. 4 and 7, it would seem that the graphene sheet setup is less sensitive to differentiating between various interaction models. This is, however, due to the fact that in this approach, we integrate over all outgoing electrons that are ejected under the graphene sheet plane, and the effects of various interaction types wash out. The detector acceptance of carbon nanotubes cuts out a narrower window in the direction of the outgoing electrons, making different couplings distinguishable. Therefore, if one would impose a similar directional cut on the outgoing electrons from the graphene sheets, one would be able to better distinguish various interaction models as well (as can be seen from Figs. 5 and 6).

Figures 8 and 9 show the angular dependence of the total event rate integrated over all electron energies for the magnetic dipole and the O_3 contact interaction, respectively. As for the case of graphene, we see that the direction of electron ejections largely tracks the DM wind for the magnetic dipole interaction, whereas it is displaced from the direction of the DM wind for O_3 contact interaction.

C. Exclusion limits and discovery potential

To compare the expected performance of CNT and graphene sheet-based experiments, we give the expected sensitivities for discovering a daily modulation signal and expected exclusion limits in the case of a null result for a 10 g-yr exposure. Figure 10 shows the expected 3σ sensitivity for the four experiments illustrated in Figs. 2 and 3 obtained with the likelihood defined in Eq. (19). Different colors correspond to different experimental setups, and various line styles correspond to a different number of background events. The solid line shows the 3σ sensitivity of discovery for ten background events θ, whereas the dashed line represents the same calculation with $\theta = 1000$ background events. The panels correspond

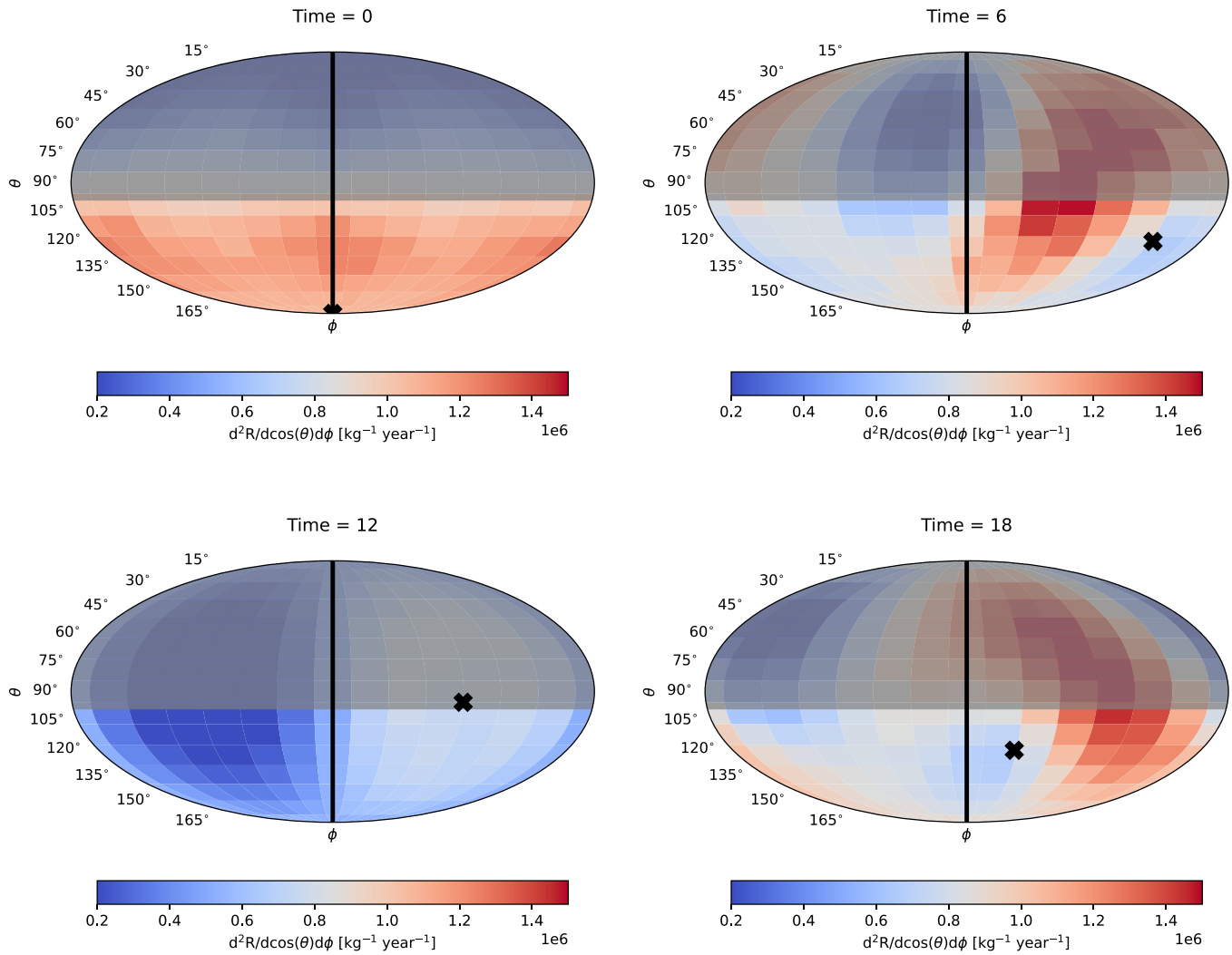

FIG. 9. Same as Fig. 6, but for a detector made of CNTs. The vertical black line corresponds to the orientation of the tube axis.

to different forms of DM-electron interactions, and the gray area is excluded by other direct-detection experiments.

We see that for the contactlike interactions, O_1 and O_3 contact, as well as for the anapole and magnetic dipole interactions, the CNT-based experiments perform considerably better than the graphene sheet-based ones. This is due to contact interactions exhibiting a considerably stronger daily modulation pattern in CNTs than in graphene sheets. Comparing the $m_\chi = 100$ MeV panels in Figs. 4 and 7, one sees that while the electric dipole and magnetic dipole have minima between $\mathscr{R}/\langle\mathscr{R}\rangle = 0.5$ and 0.7 for both CNTs and graphene sheets, the contactlike interactions have a minimum well below $\mathscr{R}/\langle\mathscr{R}\rangle = 0.5$ for CNTs and well above $\mathscr{R}/\langle\mathscr{R}\rangle = 0.5$ for graphene sheets.

At lower DM masses, graphene sheets outperform CNTs, but the difference, when compared to moving-CNTs setups, is small. The fixed-CNTs setup does, however, suffer a notable loss of sensitivity at a region between $m_\chi = 3$ and 6 MeV, depending on the interaction type. The loss of sensitivity in this mass range is due to the flattening of the daily modulation plot in Fig. 7 (given by the balancing of the two competing directional effects discussed above), where the daily modulation pattern is flatter for $m_\chi = 5$ MeV than for $m_\chi = 2$ and 10 MeV. For the electric dipole and O_1 long-range interactions, these curves are almost entirely flat, explaining why the regions of insensitivity of the fixed CNT setup in Fig. 10 are more pronounced for these interactions.

Finally, we see that with a 10 g-yr exposure, there is a sizable nonexcluded parameter space in which DM can be discovered at 3σ confidence limit in the event of $\theta = 10$ background events. This is true in particular for the moving-CNTs setup. Increasing the number of background events to $\theta = 1000$ shrinks this parameter space severely, still leaving tiny patches of allowed parameter space in which DM can be discovered. An exception to this is the O_3 contact interaction, which induces a very strong daily modulation signal in CNTs at DM masses above 5 MeV, leaving a vast allowed parameter space in which DM can be discovered at 3σ even with $\theta = 1000$ background events.

In Fig. 11, we show a contour around the $\theta = 10$ reaches shown previously in Fig. 10. This contour is obtained from Eq. (20) and represents the region in which the exclusion

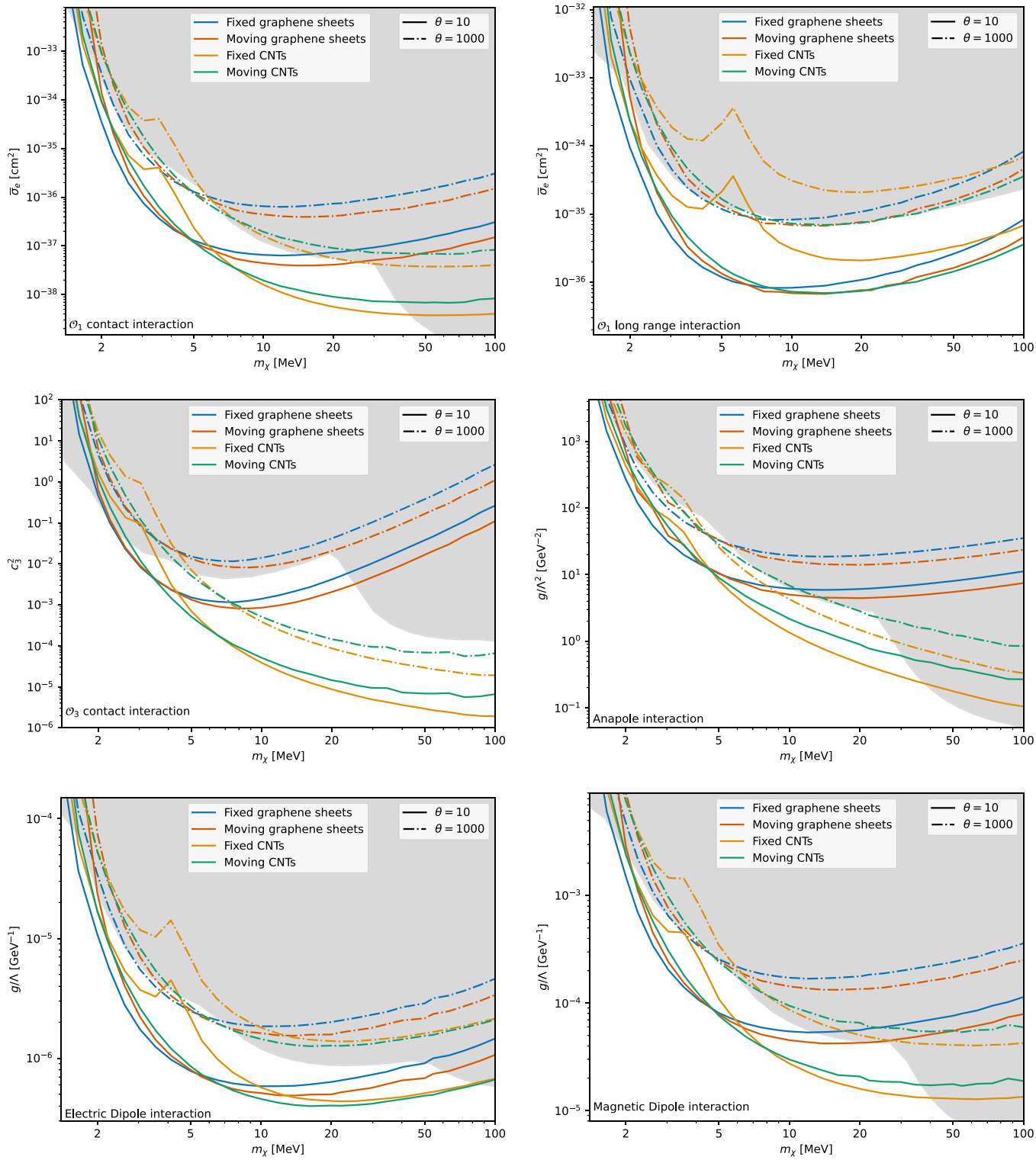

FIG. 10. Sensitivities of carbon nanotube detection setups with a 10 g yr exposure for O_1 short range (top left), O_1 long range (top right), O_3 short range (center left), anapole (center right), electric dipole (bottom left), and magnetic dipole (bottom right) interactions. The interaction strength of these DM electron interactions is characterized by dimensionless quantities such as effective operator couplings c, coupling strengths g, and/or the energy scale Λ at which the interaction is generated. The lines correspond to 3σ discovery significance, where parameter points above the line are expected to be discovered with more than 3σ significance in the event of θ number of background events. The line styles correspond to different numbers of background events, with the solid line corresponding to $\theta = 10$ background events, and the dash-dotted line corresponding to $\theta = 1000$ background events. The different colors correspond to the different experimental setups shown in Figs. 2 and 3. The gray region is already excluded by other experiments [7,9,32,35,40,42–44]. The bumps in the sensitivity curves for some of the experimental setups are due to s_+ and s_- becoming similar at these masses.

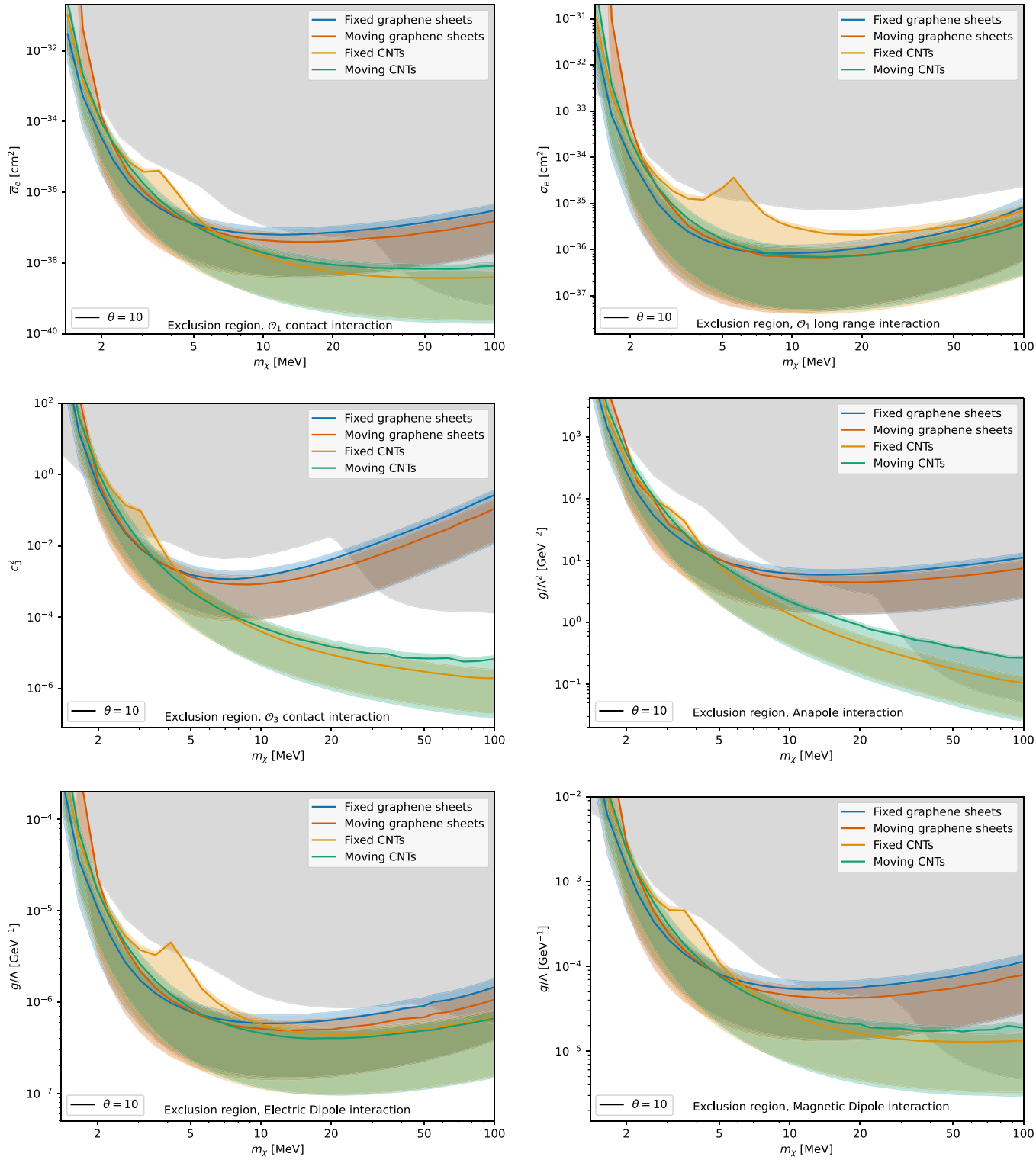

FIG. 11. As Fig. 10, with lines corresponding to where daily modulation can be established at 3σ significance for the experimental setups shown in Figs. 2 and 3, together with an envelope region whose lower border is obtained from Eq. (20) with $n_- + n_+ = 0$, and the upper border with $n_- + n_+ = \mu'(s_- + s_+) + \theta$, where $\theta = 10$ and μ' is the strength parameter corresponding to the 3σ significance line. The exposure is assumed to be 10 g yr.

limits of DM can lie. The lower edge of the contour is given by the exclusion limit in the scenario of no observed events, i.e., $n_- + n_+ = 0$, whereas the upper edge is the "worst case" scenario for $\theta = 10$, where there are still not enough DM events for discovery, and one has to resort to excluding DM having observed $n_- + n_+ = \mu'(s_- + s_+) + \theta$ events, where μ' is the value of the strength parameter at which DM can be detected at 3σ. We see that the CNT-based setups

have the potential to considerably constrain the parameter space for all the considered models in the case of a null result.

We stress here that the 3σ discovery limits reported in this section should be understood as "median" values subject to statistical fluctuations. While properly assessing the impact of statistical fluctuations on our projections would require Monte Carlo simulations that go beyond the scope of this work, we expect that the reported sensitivity limits would vary within a factor of a few because of statistical fluctuations in the number of observed events. This statement is supported by the results found in Ref. [45] (see Fig. 17) and Ref. [46] (see Fig. 5), where a Monte Carlo analysis of the impact of statistical fluctuations on the discovery limits in daily modulation experiments is performed.

VI. SUMMARY AND CONCLUSION

In summary, we performed a comprehensive theoretical study of graphene- and carbon-nanotube-based targets as materials for the directional detection of DM, identifying the discovery potential and directionality for various types of interaction, as well as exploring different detector device setups.

Based on our findings in Paper I, we chose DFT as our framework for obtaining the electronic structure of the graphene and CNT targets. We then modeled the DM-SM interaction within the generalized effective operator approach [32,35], and we described the ejected final-state electrons as free-electron plane waves. The use of plane-wave final states allowed us to reduce the formalism previously employed in [35] for 3D semiconductor targets, and describe all the operators listed in Table I with a single-crystal response, Eq. (2).

Our main findings are as follows:

(i) The directionality and characteristic spatial distribution of DM-induced electronic ejections from graphene and CNTs can be used to exclude many potential background sources, which in turn enables the origin of the observed signal to be identified. In addition to either confirming or disproving the DM-origin hypothesis, the distribution yields important information about the nature of the DM candidate. In particular, different DM couplings and masses produce different angular distributions of the final-state electrons allowing for an interaction-type distinction once a signal has been established.

(ii) The reach of the graphene- and CNT-based experiments currently under consideration is not expected to push the detection reach many orders of magnitude beyond its current experimental limits [7,9,32,35,42–44]. It will help, however, to resolve the observed signal excesses of other experiments in that mass range.

(iii) In general, CNTs exhibit a slightly better detection reach than graphene sheets, with moving CNT-based detectors with the two detector arms oriented back-to-back, and fixed CNTs facing toward the DM wind being particularly promising. Detector sensitivities depend heavily on the candidate mass and coupling type, and for a particular target material choice, one can switch between operation regimes in order to cover the largest area of the possible DM parameter space or to probe one specific DM candidate with more precision.

(iv) The test statistics in the treatment of the measured data differ depending on whether a 3σ modulation has been established or not. In the first case, the reach of the detector is given by the modulation of the signal, and, in the latter, it is the absolute number of observed events and the "null result" of modulation that determines the achieved exclusion limits. We provide a quantification of the difference for the considered detector designs at an exposure of 10 g-yr.

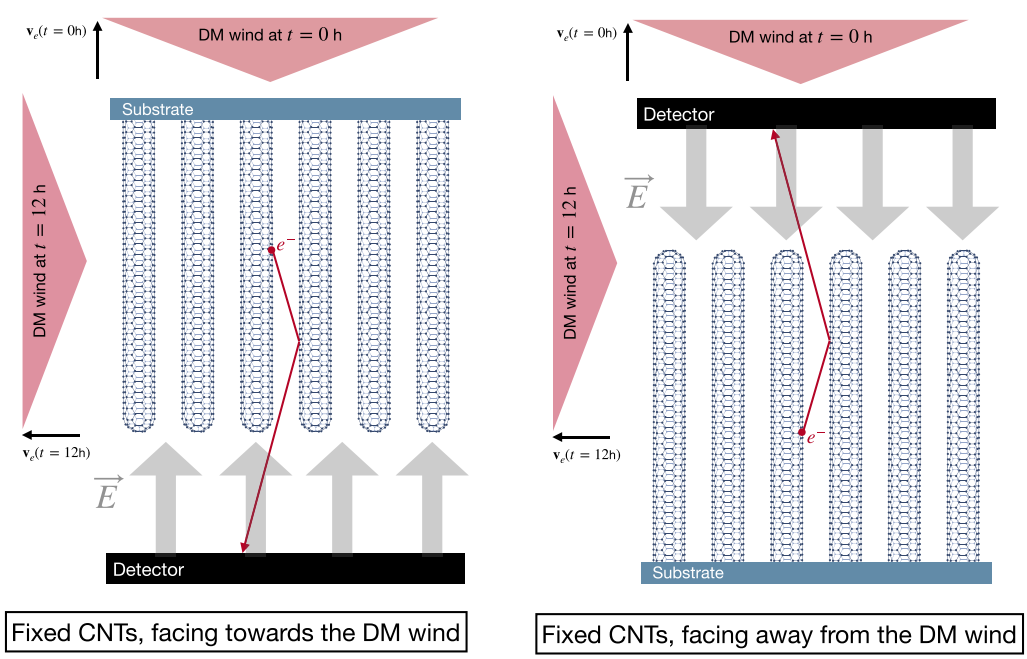

FIG. 12. Illustrations of fixed CNT setups. The left panel was already shown in Fig. 3 (left) and is repeated here for comparison.

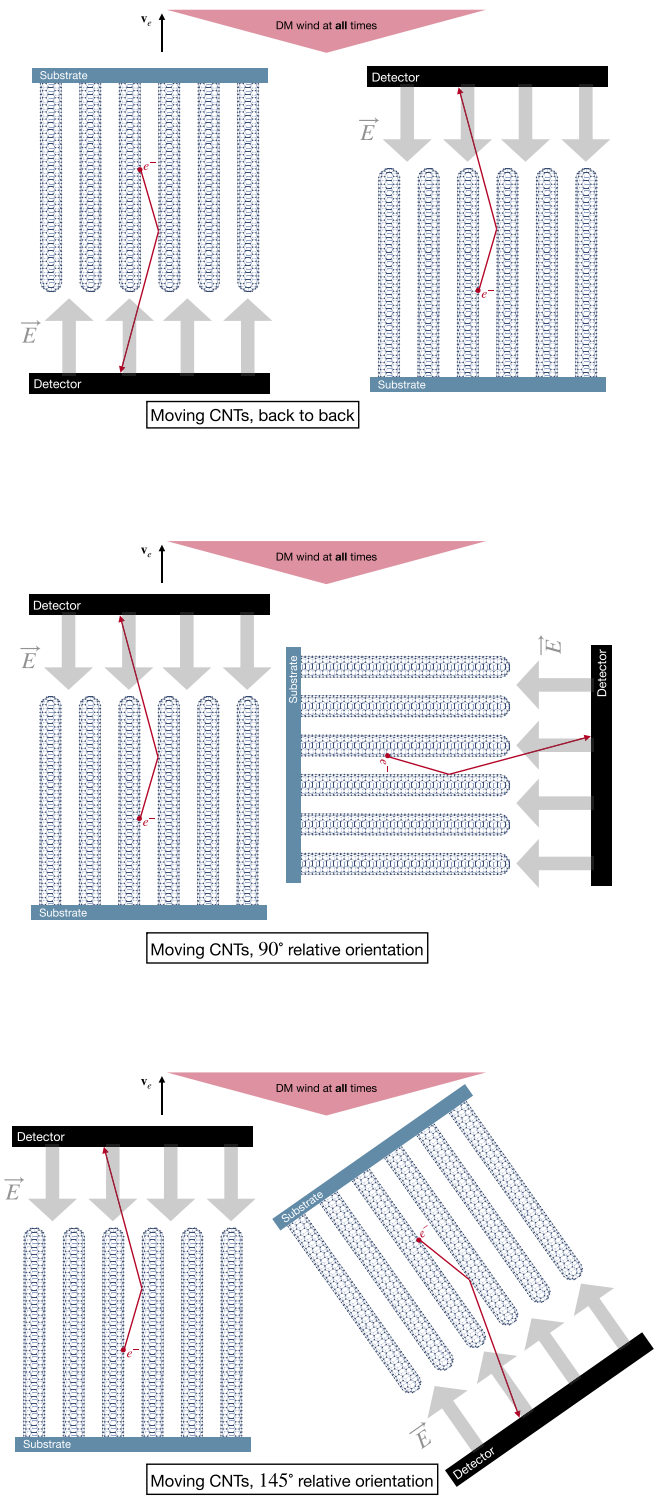

FIG. 13. Illustrations of moving CNT setups considered in this Appendix. The top panel was already shown in Fig. 3 (right) and is repeated here for comparison.

We hope that our analysis is useful in the optimization of graphene- and CNT-based detectors currently under consideration, and motivates consideration of other 2D materials for directional detection of light dark matter via electronic ejection.

An updated version of the QEDARK-EFT tool that was developed for electron ejections from two-dimensional targets will be made available at the time of publication [40].

ACKNOWLEDGMENTS

The authors thank Francesco Pandolfi and Christopher G. Tully for valuable discussions on the experimental setups. R.C. and T.E. acknowledge support from the Knut and Alice Wallenberg project grant Light Dark Matter (Dnr. KAW 2019.0080). Furthermore, R.C. acknowledges support from individual research grants from the Swedish Research Council, Dnr. 2018-05029, and Dnr. 2022-04299. T.E. was also supported by the Knut and Alice Wallenberg Foundation (PI, Jan Conrad). N.A.S. and M.M. were supported by the ETH Zürich and by the European Research Council (ERC) under the European Union's Horizon 2020 research and innovation program Grant Agreement No. 810451. T.E. thanks the Theoretical Subatomic Physics group at Chalmers University of Technology for its hospitality.

APPENDIX A: COMPARISON OF CNT-BASED SETUPS

When constructing CNT-based experiments, the performance is influenced by the orientation of the detectors. In the main body of the text, we considered two CNT-based experiments shown in Fig. 3, "Fixed CNTs facing towards the DM wind" and "Moving CNTs, back to back." We illustrate other possible setups, "Fixed CNTs facing away from the DM wind," "Moving CNTs, 90° relative orientation," and "Moving CNTs, 145° relative orientation" in Figs. 12 and 13. The latter is tailored to have one detector hit the peak around $t = 6$ h present for low DM masses in Fig. 7, while the other detector faces away from the DM wind. The performance of these setups is shown in Figs. 14 and 15.

APPENDIX B: EXPANDED MATRIX ELEMENT

For convenience, here we include the explicit free-particle response function R_{free} from Eq. (1) as taken from the Appendix of Paper I.

To avoid making the expressions too large, we divide R_{free} into three separate terms,

$$R_{\text{free}} = \overline{|\mathcal{M}|^2} + 2m_e \overline{\text{Re}\left[\mathcal{M}(\nabla_{\boldsymbol{\ell}}\mathcal{M}^*)_{\boldsymbol{\ell}=0} \cdot \frac{\mathbf{q}-\mathbf{k}'}{m_e}\right]} + m_e^2 \overline{\left|(\nabla_{\boldsymbol{\ell}}\mathcal{M})_{\boldsymbol{\ell}=0} \cdot \frac{\mathbf{q}-\mathbf{k}'}{m_e}\right|^2}, \tag{B1}$$

where $\mathbf{q}$ is the momentum transfer, m_e is the electron mass, $\mathbf{k}'$ is the final-state electron momentum, and $\boldsymbol{\ell}$ is the initial-state electron momentum. The individual terms can then be

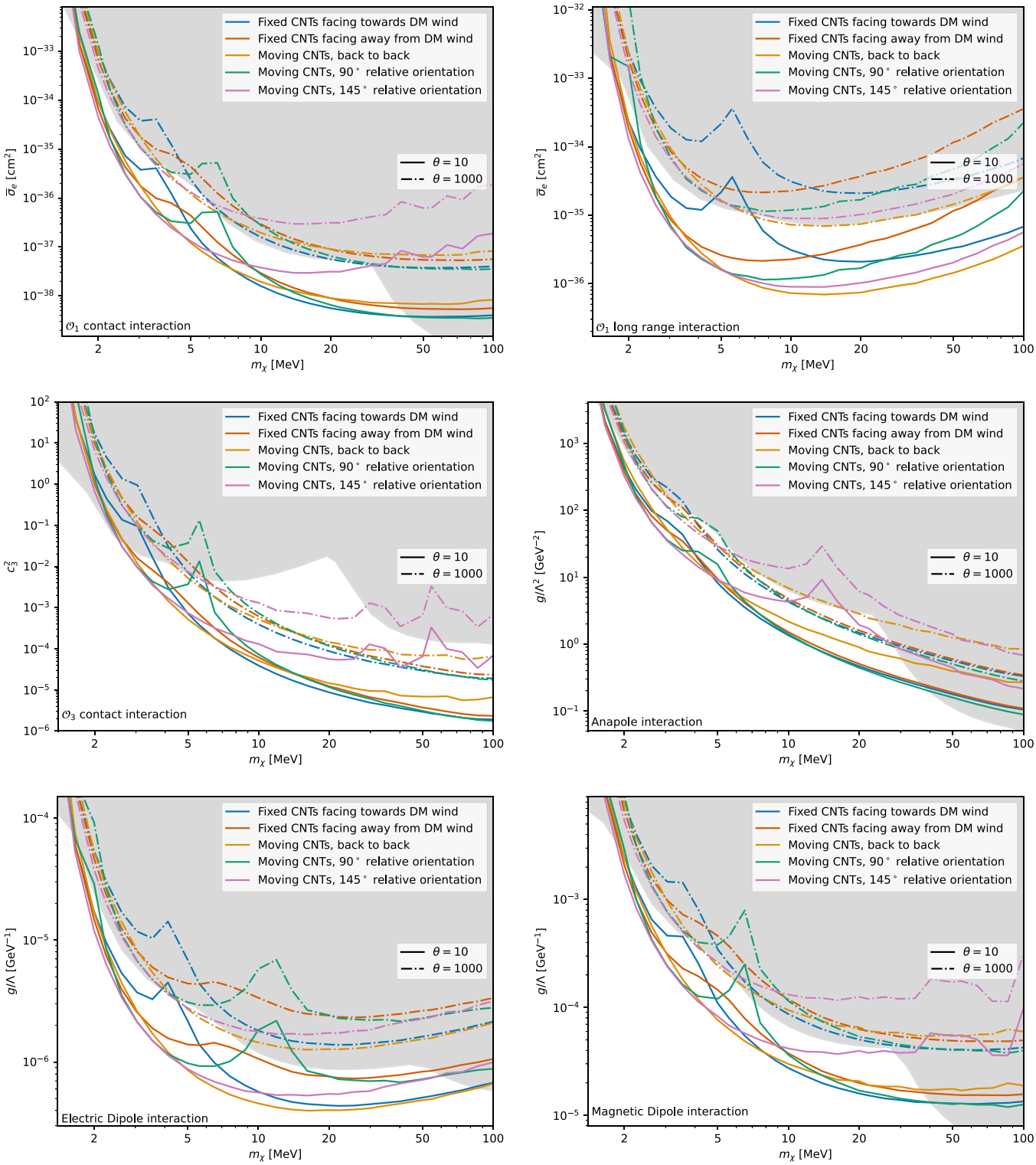

FIG. 14. Same as Fig. 10 but for the CNT-based setups illustrated in Figs. 12 and 13.

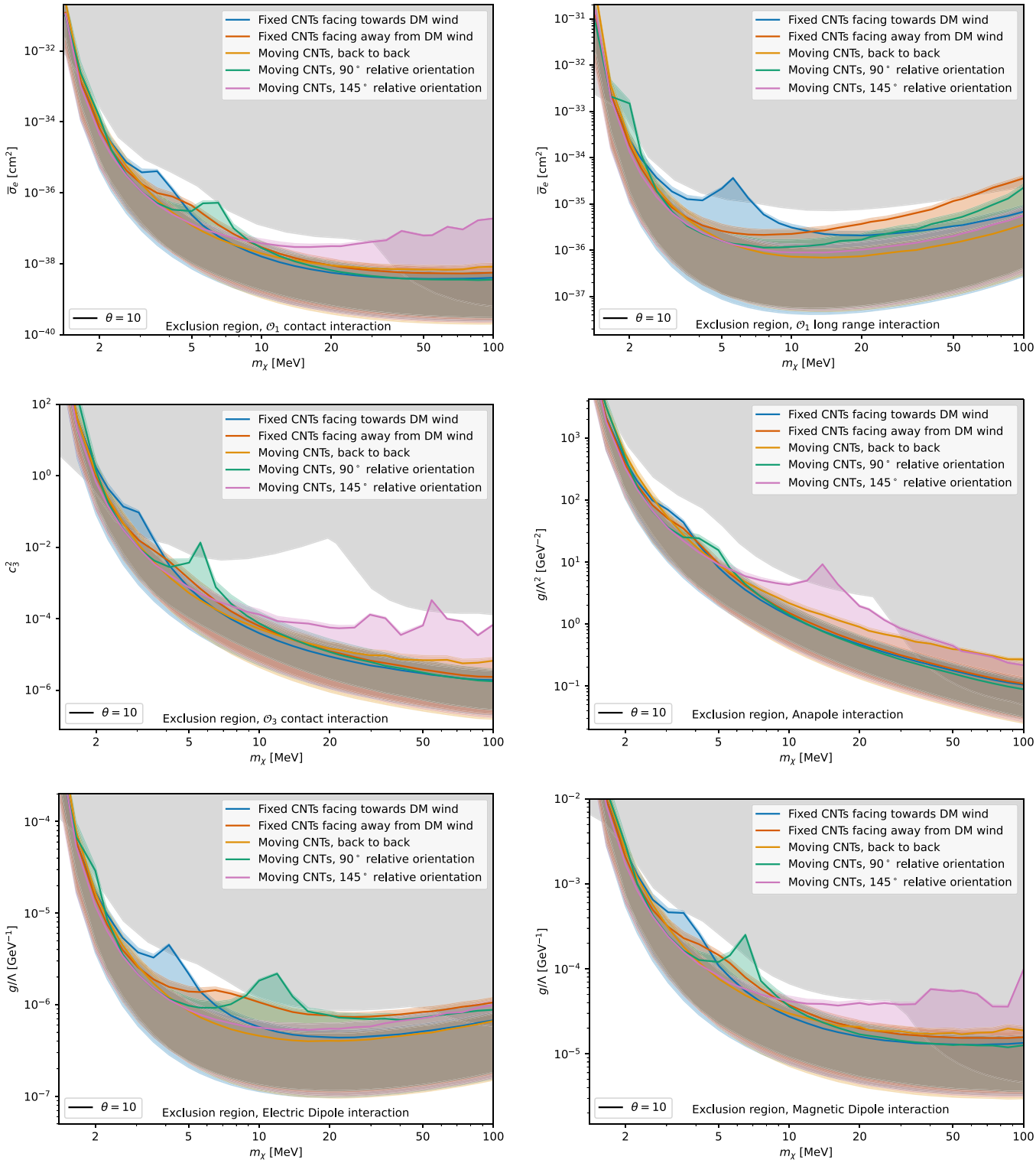

FIG. 15. Same as Fig. 11 but for the CNT based setups illustrated in Figs. 12 and 13.

expressed as

$$\overline{|\mathcal{M}|^2} = c_1^2 + \frac{c_3^2}{4}\left(\frac{\mathbf{q}}{m_e}\times\mathbf{v}_{\rm el}^{\perp}\right)^2 + \frac{c_7^2}{4}(\mathbf{v}_{\rm el}^{\perp})^2 + \frac{c_{10}^2}{4}\left(\frac{\mathbf{q}}{m_e}\right)^2 + \frac{j_\chi(j_\chi+1)}{12}\Bigg\{3c_4^2 + \left(4c_5^2 - 2c_{12}c_{15}\right)\left(\frac{\mathbf{q}}{m_e}\times\mathbf{v}_{\rm el}^{\perp}\right)^2 + c_6^2\left(\frac{\mathbf{q}}{m_e}\right)^4 + \left(4c_8^2 + 2c_{12}^2\right)(\mathbf{v}_{\rm el}^{\perp})^2 + \left(2c_9^2 + 4c_{11}^2 + 2c_4c_6\right)\left(\frac{\mathbf{q}}{m_e}\right)^2 + \left(c_{13}^2 + c_{14}^2\right)\left(\frac{\mathbf{q}}{m_e}\right)^2(\mathbf{v}_{\rm el}^{\perp})^2 + c_{15}^2\left(\frac{\mathbf{q}}{m_e}\right)^2\left(\frac{\mathbf{q}}{m_e}\times\mathbf{v}_{\rm el}^{\perp}\right)^2 + 2c_{13}c_{14}\left(\frac{\mathbf{q}}{m_e}\cdot\mathbf{v}_{\rm el}^{\perp}\right)\left(\frac{\mathbf{q}}{m_e}\cdot\mathbf{v}_{\rm el}^{\perp}\right)\Bigg\}, \tag{B2}$$

where $\mathbf{v}_{\rm el}^{\perp} = \mathbf{v} - \frac{\mathbf{q}}{2\mu_{\chi e}} - \frac{\boldsymbol{\ell}}{m_e}$, with $\mathbf{v}$ being the DM initial velocity in the detector rest frame and $\mu_{\chi e}$ the DM-electron reduced mass. c_i's are the effective couplings, and j_χ is the DM spin, which we set to 1/2,

$$\begin{aligned}
2m_e\overline{\mathrm{Re}\left[\mathcal{M}(\nabla_{\mathbf{p}_1}\mathcal{M}^*)_{\mathbf{p}_1=\mathbf{0}}\cdot\frac{\mathbf{q}-\mathbf{k}'}{m_e}\right]} = &\left[\frac{c_3^2}{2}\left(\left(\frac{\mathbf{q}}{m_e}\cdot\mathbf{v}_{\rm el}^{\perp}\right)\frac{\mathbf{q}}{m_e} - \left(\frac{\mathbf{q}}{m_e}\right)^2\mathbf{v}_{\rm el}^{\perp}\right) - \frac{c_7^2}{2}\mathbf{v}_{\rm el}^{\perp}\right]\cdot\frac{\mathbf{q}-\mathbf{k}'}{m_e} \\
&+ \frac{j_\chi(j_\chi+1)}{6}\Bigg\{\Bigg[\left(4c_5^2 + c_{15}^2\left(\frac{\mathbf{q}}{m_e}\right)^2\right)\left(\left(\frac{\mathbf{q}}{m_e}\cdot\mathbf{v}_{\rm el}^{\perp}\right)\frac{\mathbf{q}}{m_e} - \left(\frac{\mathbf{q}}{m_e}\right)^2\mathbf{v}_{\rm el}^{\perp}\right) \\
&- \left(4c_8^2 + 2c_{12}^2 + \left(c_{13}^2 + c_{14}^2\right)\left(\frac{\mathbf{q}}{m_e}\right)^2\right)\mathbf{v}_{\rm el}^{\perp}\Bigg]\cdot\frac{\mathbf{q}-\mathbf{k}'}{m_e} \\
&- 2c_{12}c_{15}\left(\left(\frac{\mathbf{q}}{m_e}\cdot\mathbf{v}_{\rm el}^{\perp}\right)\frac{\mathbf{q}}{m_e} - \left(\frac{\mathbf{q}}{m_e}\right)^2\mathbf{v}_{\rm el}^{\perp}\right)\cdot\frac{\mathbf{q}-\mathbf{k}'}{m_e} \\
&- 2c_{13}c_{14}\left(\frac{\mathbf{q}}{m_e}\cdot\mathbf{v}_{\rm el}^{\perp}\right)\frac{\mathbf{q}}{m_e}\cdot\frac{\mathbf{q}-\mathbf{k}'}{m_e}\Bigg\},
\end{aligned} \tag{B3}$$

and

$$\begin{aligned}
m_e^2\overline{\left|(\nabla_{\mathbf{p}_1}\mathcal{M})_{\mathbf{p}_1=0}\cdot\frac{\mathbf{q}-\mathbf{k}'}{m_e}\right|^2} = &\left(\frac{c_3^2}{4}\left(\frac{\mathbf{q}}{m_e}\right)^2 + \frac{c_7^2}{4}\right)\left(\frac{\mathbf{q}-\mathbf{k}'}{m_e}\right)^2 - \frac{c_3^2}{4}\left(\frac{\mathbf{q}}{m_e}\cdot\frac{\mathbf{q}-\mathbf{k}'}{m_e}\right)^2 \\
&+ \frac{j_\chi(j_\chi+1)}{12}\Bigg\{\left(\frac{\mathbf{q}-\mathbf{k}'}{m_e}\right)^2\left[\left(4c_5^2 + c_{13}^2 + c_{14}^2 - 2c_{12}c_{15}\right)\left(\frac{\mathbf{q}}{m_e}\right)^2 + 4c_8^2 + 2c_{12}^2 + c_{15}^2\left(\frac{\mathbf{q}}{m_e}\right)^4\right] \\
&+ \left(\frac{\mathbf{q}}{m_e}\cdot\frac{\mathbf{q}-\mathbf{k}'}{m_e}\right)^2\left[-4c_5^2 - c_{15}^2\left(\frac{\mathbf{q}}{m_e}\right)^2 + 2c_{12}c_{15} + 2c_{13}c_{14})\right]\Bigg\}.
\end{aligned} \tag{B4}$$

Furthermore, to rewrite the above equations, one can use the following relations:

$$\left(\frac{\mathbf{q}}{m_e}\times\mathbf{v}_{\rm el}^{\perp}\right)^2 = \left(\frac{\mathbf{q}}{m_e}\right)^2(\mathbf{v}_{\rm el}^{\perp})^2 - \left(\frac{\mathbf{q}}{m_e}\cdot\mathbf{v}_{\rm el}^{\perp}\right)^2, \tag{B5}$$

$$(\mathbf{v}_{\rm el}^{\perp})^2|_{\boldsymbol{\ell}=0} = \mathbf{v}^2 + \frac{\mathbf{q}^2}{4\mu_{\chi e}^2}\frac{m_\chi - m_e}{m_e + m_\chi} - \frac{\Delta E_e}{\mu_{\chi e}}, \tag{B6}$$

$$(\mathbf{v}_{\rm el}^{\perp}\cdot\mathbf{q})|_{\boldsymbol{\ell}=0} = \Delta E_e - \frac{\mathbf{q}^2}{2m_e}, \tag{B7}$$

$$\mathbf{v}_{\rm el}^{\perp}|_{\boldsymbol{\ell}=0} = \mathbf{v} - \frac{\mathbf{q}}{2\mu_{\chi e}}, \tag{B8}$$

where ΔE_e is the energy transferred to the target electron.

[1] M. Battaglieri *et al.*, US Cosmic Visions: New Ideas in Dark Matter 2017; Community Report, FERMILAB-CONF-17-282-AE-PPD-T, arXiv:1707.04591 [hep-ph].

[2] A. Drukier and L. Stodolsky, Principles and applications of a neutral current detector for neutrino physics and astronomy, Phys. Rev. D **30**, 2295 (1984).

[3] M. W. Goodman and E. Witten, Detectability of certain dark matter candidates, Phys. Rev. D **31**, 3059 (1985).
[4] R. Essig, J. Mardon, and T. Volansky, Direct detection of Sub-GeV dark matter, Phys. Rev. D **85**, 076007 (2012).
[5] R. Essig, M. Fernandez-Serra, J. Mardon, A. Soto, T. Volansky, and T.-T. Yu, Direct Detection of sub-GeV Dark Matter with Semiconductor Targets, J. High Energy Phys. 05 (2016) 046.
[6] P. Agnes *et al.* (DarkSide Collaboration), Constraints on sub-GeV dark-matter–electron scattering from the DarkSide-50 experiment, Phys. Rev. Lett. **121**, 111303 (2018).
[7] R. Essig, A. Manalaysay, J. Mardon, P. Sorensen, and T. Volansky, First direct detection limits on sub-GeV dark matter from XENON10, Phys. Rev. Lett. **109**, 021301 (2012).
[8] R. Essig, T. Volansky, and T.-T. Yu, New constraints and prospects for sub-GeV dark matter scattering off electrons in xenon, Phys. Rev. D **96**, 043017 (2017).
[9] E. Aprile *et al.* (XENON Collaboration), Light dark matter search with ionization signals in XENON1T, Phys. Rev. Lett. **123**, 251801 (2019).
[10] P. W. Graham, D. E. Kaplan, S. Rajendran, and M. T. Walters, Semiconductor probes of light dark matter, Phys. Dark Univ. **1**, 32 (2012).
[11] S. K. Lee, M. Lisanti, S. Mishra-Sharma, and B. R. Safdi, Modulation effects in dark matter-electron scattering experiments, Phys. Rev. D **92**, 083517 (2015).
[12] M. Crisler, R. Essig, J. Estrada, G. Fernandez, J. Tiffenberg, M. Sofoharo, T. Volansky, and T.-T. Yu (SENSEI Collaboration), SENSEI: First direct-detection constraints on sub-GeV dark matter from a surface run, Phys. Rev. Lett. **121**, 061803 (2018).
[13] R. Agnese *et al.* (SuperCDMS), First dark matter constraints from a superCDMS single-charge sensitive detector, Phys. Rev. Lett. **121**, 051301 (2018); **122**, 069901 (2019).
[14] O. Abramoff, L. Barak, I. M. Bloch, L. Chaplinsky, M. Crisler, Dawa, A. Drlica-Wagner, R. Essig, J. Estrada, E. Etzion *et al.* (SENSEI), SENSEI: Direct-detection constraints on sub-GeV dark matter from a shallow underground run using a prototype skipper CCD, Phys. Rev. Lett. **122**, 161801 (2019).
[15] A. Aguilar-Arevalo, D. Amidei, D. Baxter, G. Cancelo, B. A. Cervantes Vergara, A. E. Chavarria, E. Darragh-Ford, J. R. T. de Mello Neto, J. C. D'Olivo, J. Estrada *et al.* (DAMIC Collaboration), Constraints on light dark matter particles interacting with electrons from DAMIC at SNOLAB, Phys. Rev. Lett. **123**, 181802 (2019).
[16] D. W. Amaral *et al.* (SuperCDMS), Constraints on low-mass, relic dark matter candidates from a surface-operated SuperCDMS single-charge sensitive detector, Phys. Rev. D **102**, 091101 (2020).
[17] E. Andersson, A. Bökmark, R. Catena, T. Emken, H. K. Moberg, and E. Åstrand, Projected sensitivity to sub-GeV dark matter of next-generation semiconductor detectors, J. Cosmol. Astropart. Phys. **2020**, 036 (2020).
[18] Y. Hochberg, Y. Kahn, M. Lisanti, K. M. Zurek, A. G. Grushin, R. Ilan, S. M. Griffin, Z.-F. Liu, S. F. Weber, and J. B. Neaton, Detection of sub-MeV dark matter with three-dimensional Dirac materials, Phys. Rev. D **97**, 015004 (2018).
[19] R. M. Geilhufe, F. Kahlhoefer, and M. W. Winkler, Dirac materials for sub-MeV dark matter detection: New targets and improved formalism, Phys. Rev. D **101**, 055005 (2020).
[20] Y. Hochberg, Y. Kahn, M. Lisant, C. G. Tully, and K. M. Zurek, Directional detection of dark matter with two-dimensional targets, Phys. Lett. B **772**, 239 (2017).
[21] R. M. Geilhufe, B. Olsthoorn, A. Ferella, T. Koski, F. Kahlhoefer, J. Conrad, and A. V. Balatsky, Materials informatics for dark matter detection, Phys. Status Solidi (RRL) **12**, 0293 (2018).
[22] L. M. Capparelli, G. Cavoto, D. Mazzilli, and A. D. Polosa, Directional dark matter searches with carbon nanotubes, Phys. Dark Univ. **9-10**, 24 (2015); **11**, 79 (2016).
[23] G. Cavoto, E. N. M. Cirillo, F. Cocina, J. Ferretti, and A. D. Polosa, WIMP detection and slow ion dynamics in carbon nanotube arrays, Eur. Phys. J. C **76**, 349 (2016).
[24] G. Cavoto, F. Luchetta, and A. D. Polosa, Sub-GeV dark matter detection with electron recoils in carbon nanotubes, Phys. Lett. B **776**, 338 (2018).
[25] G. Cavoto, M. G. Betti, C. Mariani, F. Pandolfi, A. D. Polosa, I. Rago, and A. Ruocco, Carbon nanotubes as anisotropic target for dark matter, J. Phys.: Conf. Ser. **1468**, 012232 (2020).
[26] S. Betts *et al.*, Development of a relic neutrino detection experiment at PTOLEMY: Princeton tritium observatory for light, early-universe, massive-neutrino yield, in Community Summer Study 2013: Snowmass on the Mississippi, arXiv:1307.4738 [astro-ph.IM].
[27] E. Baracchini *et al.* (PTOLEMY), PTOLEMY: A proposal for thermal relic detection of massive neutrinos and directional detection of MeV dark matter, arXiv:1808.01892 [physics.ins-det].
[28] A. Apponi *et al.* (PTOLEMY Collaboration), Heisenberg's uncertainty principle in the PTOLEMY project: A theory update, Phys. Rev. D **106**, 053002 (2022).
[29] A. Apponi, G. Cavoto, C. Mariani, F. Pandolfi, I. Rago, A. Ruocco, C. Tully, and F. Zhao, Carbon nanostructures for directional light dark matter detection, PoS **ICHEP2020**, 648 (2021).
[30] F. Pandolfi, I. Rago, G. Cavoto, C. Mariani, A. Apponi, and A. Ruocco, The dark-PMT: A novel directional light dark matter detector based on vertically-aligned carbon nanotubes, Nucl. Instrum. Methods Phys. Res., Sect. A **1050**, 168116 (2023).
[31] R. Catena, T. Emken, M. Matas, N. A. Spaldin, and E. Urdshals, preceding paper, Direct searches for general dark matter-electron interactions with graphene detectors: Part I. Electronic structure calculations, Phys. Rev. Res. **5**, 043257 (2023).
[32] R. Catena, T. Emken, N. A. Spaldin, and W. Tarantino, Atomic responses to general dark matter-electron interactions, Phys. Rev. Res. **2**, 033195 (2020).
[33] Z. Feng, X. Zhang, Y. Sakurai, Z. Wang, H. Li, and H. Hu, Compton profile of few-layer graphene investigated by electron energy-loss spectroscopy, Sci. Rep. **9**, 1 (2019).
[34] P. E. Trevisanutto, C. Giorgetti, L. Reining, M. Ladisa, and V. Olevano, Ab initio *GW* many-body effects in graphene, Phys. Rev. Lett. **101**, 226405 (2008).
[35] R. Catena, T. Emken, M. Matas, N. A. Spaldin, and E. Urdshals, Crystal responses to general dark matter-electron interactions, Phys. Rev. Res. **3**, 033149 (2021).
[36] D. Baxter *et al.*, Recommended conventions for reporting results from direct dark matter searches, Eur. Phys. J. C **81**, 907 (2021).
[37] P. Giannozzi, S. Baroni, N. Bonini, M. Calandra, R. Car, C. Cavazzoni, D. Ceresoli, G. L. Chiarotti, M. Cococcioni, I. Dabo *et al.*, Quantum espresso: A modular and open-source software

project for quantum simulations of materials, J. Phys.: Condens. Matter **21**, 395502 (2009).

[38] P. Giannozzi, O. Andreussi, T. Brumme, O. Bunau, M. B. Nardelli, M. Calandra, R. Car, C. Cavazzoni, D. Ceresoli, M. Cococcioni, N. Colonna, I. Carnimeo, A. D. Corso, S. de Gironcoli, P. Delugas, R. A. DiStasio Jr, A. Ferretti, A. Floris, G. Fratesi, G. Fugallo *et al.*, Advanced capabilities for materials modelling with quantum ESPRESSO, J. Phys.: Condens. Matter **29**, 465901 (2017).

[39] P. Giannozzi, O. Baseggio, P. Bonfà, D. Brunato, R. Car, I. Carnimeo, C. Cavazzoni, S. de Gironcoli, P. Delugas, F. Ferrari Ruffino, A. Ferretti, N. Marzari, I. Timrov, A. Urru, and S. Baroni, Quantum espresso toward the exascale, J. Chem. Phys. **152**, 154105 (2020).

[40] E. Urdshals and M. Matas, QEdark-EFT (0.1.0), Zenodo (2021).

[41] G. Cowan, K. Cranmer, E. Gross, and O. Vitells, Asymptotic formulae for likelihood-based tests of new physics, Eur. Phys. J. C **71**, 1554 (2011); **73**, 2501 (2013).

[42] L. Barak, I. M. Bloch, M. Cababie, G. Cancelo, L. Chaplinsky, F. Chierchie, M. Crisler, A. Drlica-Wagner, R. Essig, J. Estrada, E. Etzion, G. F. Moroni, D. Gift, S. Munagavalasa, A. Orly, D. Rodrigues, A. Singal, M. S. Haro, L. Stefanazzi, J. Tiffenberg, S. Uemura, T. Volansky, T. T. Yu, (SENSEI), SENSEI: Direct-detection results on sub-GeV dark matter from a new skipper CCD, Phys. Rev. Lett. **125**, 171802 (2020).

[43] J. Angle, E. Aprile, F. Arneodo, L. Baudis, A. Bernstein, A. I. Bolozdynya, L. C. C. Coelho, C. E. Dahl, L. De Viveiros, A. D. Ferella, L. M. P. Fernandes, S. Fiorucci, R. J. Gaitskell, K. L. Giboni, R. Gomez, R. Hasty, L. Kastens, J. Kwong, J. A. M. Lopes, N. Madden, A. Manalaysay, A. Manzur, D. N. McKinsey, M. E. Monzani, K. Ni, U. Oberlack, J. Orboeck, G. Plante, R. Santorelli, J. M. F. dos Santos, S. Schulte, P. Shagin, T. Shutt, P. Sorensen, C. Winant, M. Yamashita (XENON10), A search for light dark matter in XENON10 data, Phys. Rev. Lett. **107**, 051301 (2011); **110**, 249901(E) (2013).

[44] E. Aprile *et al.* (XENON Collaboration), Emission of single and few electrons in XENON1T and limits on light dark matter, Phys. Rev. D **106**, 022001 (2022).

[45] S. Griffin, S. Knapen, T. Lin, and K. M. Zurek, Directional detection of light dark matter with polar materials, Phys. Rev. D **98**, 115034 (2018).

[46] A. Coskuner, T. Trickle, Z. Zhang, and K. M. Zurek, Directional detectability of dark matter with single phonon excitations: Target comparison, Phys. Rev. D **105**, 015010 (2022).